Forecasting Selectivity of Au-based Partial Oxidation Catalysts via Temperature Programmed Desorption Studies on the Au(111) Model Catalyst

A THESIS
SUBMITTED TO THE DEPARTMENT OF CHEMISTRY AND
THE GRADUATE SCHOOL OF ENGINEERING AND SCIENCE OF
BILKENT UNIVERSITY
IN PARTIAL FULFILLMENT OF THE REQUIREMENTS
FOR THE DEGREE
OF
MASTER OF SCIENCE

by

SYED ASAD ALI SHAH

September, 2014

To My Family

And

Zarne

I certify that I have read this thesis and in my opinion it is fully adequate, in scope and quality, as a thesis of the degree of Master of Science

_____

Asst. Prof. Emrah ÖZENSOY (Supervisor)

I certify that I have read this thesis and in my opinion it is fully adequate, in scope and quality, as a thesis of the degree of Master of Science

_____

Prof. Dr. Şefik SÜZER

I certify that I have read this thesis and in my opinion it is fully adequate, in scope and quality, as a thesis of the degree of Master of Science

_____

Prof. Dr. Oğuz GÜLSEREN

Approved for the Graduate School of Engineering and Science

_____

Prof. Dr. Levent ONURAL

Director of Graduate School of Engineering and Science

Forecasting Selectivity of Au-based Partial Oxidation Catalysts via Temperature Programmed Desorption Studies on the Au(111) Model Catalyst

SYED ASAD ALI SHAH

M.S in Chemistry

Supervisor: Assistant Prof. Dr. Emrah ÖZENSOY
September, 2014

ABSTRACT

Gold-based heterogeneous catalysts have attracted significant attention due to their selective partial oxidation capabilities which are comparable to that of the industrial homogeneous benchmark catalysts. In the current study, a planar Au(111) single crystal model catalyst surface was utilized to understand the behavior of different organic compounds (alcohols, aldehydes, esters etc.) in conjunction to the partial oxidation reactions. Stability of different organic compounds were investigated on the Clean Au(III) surface. The stability of a particular organic compound on the Au(III) model catalyst surface was found to be closely related to the variety of generated products. Surface sensitive analytical techniques such as Temperature Programmed Desorption (TPD) and Low Energy Electron Diffraction (LEED) were used to investigate the interaction of organic compounds with the clean Au(111) single crystal surfaces under ultra-high vacuum (UHV) conditions. Organic compounds were dosed onto atomically clean Au(III) surfaces at the liquid nitrogen temperature. All organic compounds desorbed non-dissociatively on the clean Au(111) surface. All organic compounds reveal monolayer and multilayer desorption signals but in the case of aldehydes, desorption is quite different, as they lead to polymerization on the surface with high desorption temperatures. Zeroth order desorption kinetics was observed for multilayers, while 1^{st} order desorption was seen for the monolayer. In most cases, the multilayer feature can be observed with two distinct desorption peaks associated with amorphous and crystalline phases. In this work, it is confirmed that majority of the studied compounds have relatively low adsorption energies on Au(111). The species with lower desorption energies on Au(111) tend to undergo partial oxidation rather than total oxidation. Thus, desorption energy appears as an important descriptor for predicting the extent of oxidation in partial/total oxidation in oxidative coupling reactions.

ÖZET

Au-Tabanlı Kısmi Yükselteme Katalizörlerinin Au(111) Model Katalizörü Yüzeyinde Gerçekleştirilen Sıcaklık Programlı Desorpsiyon Çalışmaları Yardımıyla Seçiciliğinin Belirlenmesi

SYED ASAD ALI SHAH

Tez Danışmanı: Yrd. Doç. Emrah ÖZENSOY

Altın tabanlı heterojen katalizörlerin seçici kısmi yükseltgeme kabiliyetlerinin endüstride kullanılan homojen katalizörlerle kıyaslanabilir ölçüde olması, altın tabanlı heterojen katalizörlerinin önemini vurgulamaktadır. Mevcut çalışmada, farklı organik bileşiklerin (alkol, aldehit, ester, vb.) kısmi yükseltgeme tepkimelerindeki davranışlarını belirlemek amacıyla model katalizör olarak düzlemsel Au(111) tek kristali kullanılmıştır. Farklı organik bileşiklerin temiz Au(111) kristali yüzeyindeki kararlılıkları araştırılmıştır. Organik bileşiklerin Au(111) kristali üzerindeki kararlılığı, bu bileşiklerin farklı ürünler vermeleri bakımından önem arzetmektedir. Ultra yüksek vakum şartlarında gerçekleştirilen tepkimelerde, organik bileşikler ile temiz Au(111) kristali arasındaki etkileşimler, sıcaklık programlı desorpsiyon (TPD), x-ışını fotoelektron spektroskopisi (XPS), ve düşük enerjili elektron kırınımı (LEED) gibi yüzey hassas yöntemlerle analiz edilmiştir. Organik bileşikler, Au(111) yüzeyine sıvı azot sıcaklığında dozlanmıştır. Kullanılan bütün organik bileşikler ayrışmasız olarak yüzeyden ayrılmıştır ve bu bileşiklerin Au(111) yüzeyinde farklı davranışları saptanmıştır. Bütün organik bileşikler çoklu katman ve tek katman olmak üzere ayrı sıcaklıklarda yüzeyden ayrılmışlardır, fakat bunun yanında aldehit ve eterler yüzeyde polimerleşerek çoklu ve tekli katman dışındaki sıcaklıklarda da yüzeyden salınım göstermişlerdir. Desorpsiyon sinyalleri, çoklu katman salınımında sıfırıncı-derece salınım kinetiğine uygunken, tek katman salınım sinyalleri birinci-derece salınım kinetiğine uymaktadır. Organik bileşiklerin çoklu katman salınımlarında amorf ve kristal yapılara ait olan iki farklı sinyal elde edilmiştir. Yapılan bu çalışmada kullanılan organik bileşiklerin Au(111) yüzeyinde tutunma sürelerinin düşük olduğu gözlenmiş ve bu da ürünlerin tamamen yükseltgenmeden kısmi yükseltgenme ürünü olarak kalacağını işaret etmektedir. Gerçekleştirilen bu adsorpsiyon ve desorpsiyon tepkimeleri, kısmi yükseltgemeli eşlenme tepkimelerinin mekanizmasını aydınlatmada önemli ölçüde yardımcı olacaktır.

ACKNOWLEDGEMENT

I would like to thank to my advisor Assistant Prof. Dr. Emrah Özensoy for supporting me for the last two years and providing me with a platform for scientific studies. İ am grateful for his scientific advice and knowledge and many insightful discussions and suggestions. He was very instrumental in helping me cranking out this thesis. I should also acknowledge Prof. Dr Omer Dağ, because he is the only reason why I am here. I would like to thank my jury members, Prof. Dr. Şefik Süzer and Prof. Dr. Oğuz Gülseren for their precious time.

I am also indebted to Dr. Evgeny I. Vovk for his guidance. He helped me in growing from nothing, a very humble person, always willing to walk an extra mile.

Ph.d students Mustafa Karatok and Sean W. Mcwhorter are wonderful and generous people, and I appreciate their help during my work. Abdurrahman Türksoy and all other group members were so nice to me.

Thanks to Ebrima Tunkara for his moral support and for being a good friend during my study period.

Special thanks to the Department of Chemistry of Bilkent University for giving me an opportunity to be a part of the chemical community.

I especially thank my mom, dad and sister. They sacrificed their life savings for me and provided unconditional love and care, I would not have made it without them and their prayers.

TABLE OF CONTENTS

LIST OF FIGURES

1. INTRODUCTION

1.1 Motivation of the Current Work

The Au (111) surface has been used in this study as a substrate for the deposition of a variety of organic compounds. The inspiration of the current work comes from partial oxidation (PO) reactions on the catalytic Au surfaces. Au catalysts are highly selective towards a multitude of products in the partial oxidation of organic molecules. On the contrary, it is well known that oxidation occurs with a rather limited selectivity on most of the precious metal catalysts such as Pt [1,2] where the reaction proceeds until all of the reactants are completely and non-selectively oxidized to CO_2 (Figure 1). The lack of selectivity in a partial oxidation process can be mostly attributed to the residence time of the side products generated during the PO steps (Figure 2). Typically, a long residence time for a particular PO side product translates into a larger chance for the product molecule to be totally oxidized into CO_2. On the other hand, a PO product with a small adsorption energy and hence a short surface residence time possesses a higher chance of desorption, hence increasing the selectivity of the catalyst towards this particular product. This particular structural-functionality relationship presents the Au single crystal model catalyst surface as an ideal experimental platform to study selective partial oxidation processes. Thus in the current study, we focus on the adsorption properties of some of the relevant organic molecules on the Au(111) single crystal model catalyst surface which are reactants or side products in the partial oxidation of alcohols. Among alcohols, ethanol is particularly a cheap and a widely accessible synthetic fuel that can be directly obtained from biological resources such as cellulosic materials or sugar cane. Thus, partial oxidation of excess ethanol in the bio-fuel industry can yield commercially valuable products such as aldehydes, ketones, organic acids and esters. Therefore, fundamental studies on the surface catalytic

chemistry of alcohols in PO processes have a vast potential to provide invaluable insight into their alternative chemical utilization.

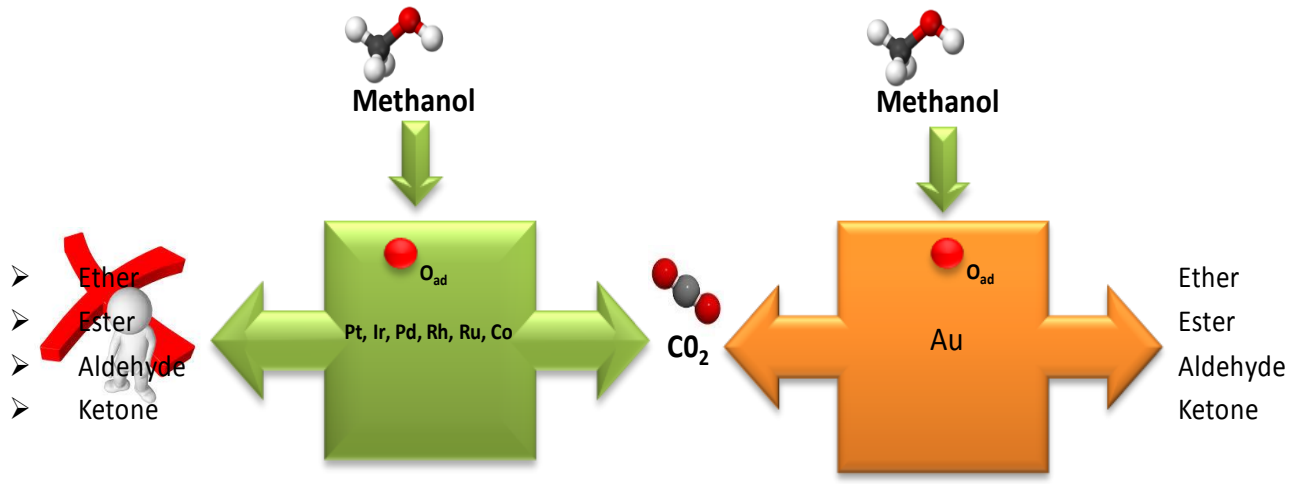

Figure 1. Partial and total oxidation reactions on various precious transition metal catalysts versus Au catalysts.

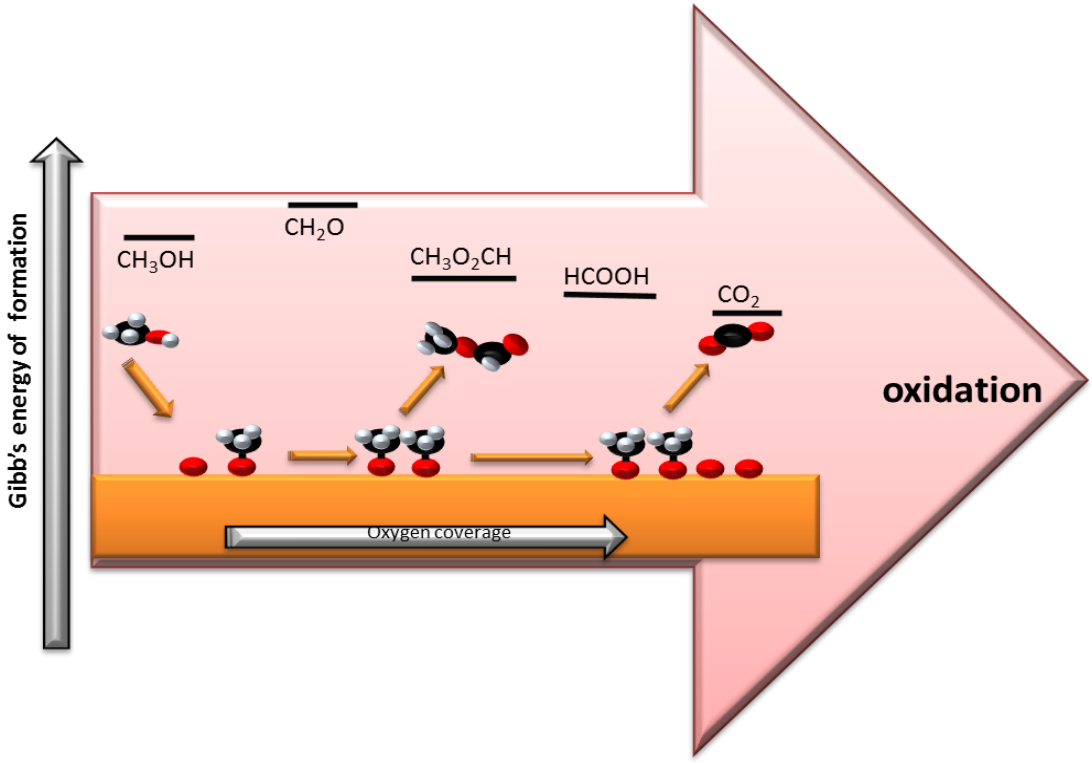

Figure 2. Reaction mechanism for the oxidation of methanol on the Au (111) model catalyst surface revealing the variety of possible reaction products [Adapted from Ref 3].

1.2 Model Catalysts and Real Life Catalysts

Model catalysts are typically comprised of single crystals, ultra-thin films or nano-particles deposited on epitaxial surfaces with surface areas on the order of 1 cm^2/g. These model experimental platforms are ubiquitous for yielding valuable information regarding the surface structure, dynamics and energetics of heterogeneous catalytic reactions [4]. The study of reaction mechanisms in a real heterogeneous catalytic system is extremely challenging due to the high pressures, elevated temperatures, dynamic flow rates; non-uniform/transient composition of reactants/products utilized in the reaction; as well as the extremely complex surface structure of the commercial catalytic architectures. Thus, the introduction of a well-defined micro kinetic model can clarify the catalytic reaction mechanism and assist us in understanding the surface properties such as atomic composition, electronic and geometric

structure and how they influence macroscopic properties such as catalytic activity and selectivity. [5,6] As mentioned above, some of the major differences between a real and a model catalytic system rest in the material complexity and catalytic reaction conditions. Real catalysts used in industry are very complex both in terms of their material properties and their operational environment. On the contrary, model catalysts are very simple, atomically well-defined and operate under ultrahigh vacuum (UHV) conditions. Thus, there exists a pressure gap [7] and a material gap [8] between conventional model catalyst studies and real catalytic investigations.

A surface science approach towards a model catalyst introduces the complex morphological and chemical features of the catalyst surface in a well-controlled and a fine-tunable manner. Heterogeneous catalytic reactions can be carried out on different atomically well-defined model catalysts with dissimilar surface structures/symmetries/compositions/defect populations/defect types in a comparative manner in an attempt to shed light on the nature and function of the active surface sites as well as the spectator sites. Such an approach also allows us to elucidate the structure sensitivity and the effect of catalytic promoters and inhibitors on the active surfaces [8]. In the last couple of decades, Au as a model catalyst has been under intense investigation due to its unique catalytic properties.

1.3 Gold in Catalysis

Historically, bulk gold has been known to be an inert material. According to Hammer and Norskov's[9] studies, there are two prominent reasons for the inertness of gold which are associated with the high probability of filling antibonding states by the adsorbates and poor orbital overlap with the adsorbate. The antibonding states of gold is lower than the Fermi level so electron is donated to the antibonding states which results in the weaker interaction between the adsorbate and the gold atoms. The extent of overlap between the orbitals of the adsorbate and the gold governs the bonding strength. Increasing overlap results in a stronger interaction. These two factors contribute towards the weak metal-adsorbate interaction and increase the barrier for dissociation [9]. The pioneering work done by Haruta et al. strongly inspired the research on catalytic Au surfaces where it was demonstrated that Au nanoparticles have an exceptional activity for the oxidation of CO even at extremely low temperatures [10]. Numerous later studies also verified that a variety of catalytic systems that are comprised of monometallic Au nanoparticles or bimetallic Au clusters supported on different reducible metal oxide surfaces are very efficient catalysts for low temperature CO oxidation [11], selective oxidation of propene to propene oxide [12], water gas shift reaction [13], NO reduction [14] and selective hydrogenation of acetylene [15]. A relatively large volume of experimental [17] and theoretical studies [18] studies in the literature have been performed in order to understand the fundamental and unusual surface science of gold catalysts. Although a complete understanding of the reaction mechanisms on catalytic Au surfaces still seems to be elusive to capture; fundamental surface science studies that can discern different active sites (e.g. particular facets on nanoparticles, low coordination sites, and interface/hetero-junction sites between Au clusters and metal-oxide support surfaces) have a potential to pave the way for a more holistic appreciation of Au-based heterogeneous catalysis.

1.3.1 Gold Nanoparticles and Clusters

There is a general consensus that the reactivity of Au nanoparticles is closely associated with the particle size. However, there exists an active and a long lasting debate in the literature on

the nature of the catalytically active Au surface sites. Several factors have been reported in the literature explaining the reactivity of the Au-containing catalytic systems such as the unique surface structure of the reducible metal oxide materials supporting Au [19], quantum size effect observed for Au clusters, charge transfer to and from the support, support-induced strain on Au nanoparticles, oxygen spill over to and from the support, variations in the oxidation state of gold [20] and the role of coordinatively unsaturated Au atoms on Au nanoparticles [21-23]. The quantum size effect is typically observed for the nanoparticles in the range of 1-10 nm that display unusual electronic structures[24]. The resulting unique physical/electronic properties are neither those of the bulk metal nor those of the molecular compound but they strongly depend on the particles size, nature of the protecting organic shell, inter-particle distance and shape of the nanoparticles [25]. Unlike the bulk (conductive) Au metal, there may exist an energy gap between the valence band and the conduction band of the Au nanoparticle. The quantum size effect is typically observed when the de Broglie wavelength of the valence electrons of the Au nanoparticle is of the same order as the size of the Au particle itself [26]. In other words, quantum effects come into existence when the particle size is small enough, e.g. below 20 nm [26]. Low coordination number is also proposed to be one of the reasons for the origin of catalytic reactivity of small Au nanoparticles (NP) exhibiting a high concentration of corner and/or edge sites [27]. Mavrikakis et al. [28] showed that molecules bind strongly at steps rather than terraces. Lemire et al. [29] showed that the adsorption of CO is stronger on small NPs as compared to larger ones, suggesting that CO adsorption is sensitive to the presence/density of under-coordinated Au atoms rather than the sole particle dimensions.

The important role of particle size on catalytic activity is apparent, however investigation of catalytic Au systems in the sub-nanometer scale is technically quite challenging as a uniform cluster size distribution (i.e. a uniform Au dispersion) is hard to achieve and characterization of small gold clusters made of only a few gold atoms under reaction (i.e. in-situ) conditions involves serious technical restrictions. Nevertheless, the recent improvements in the characterization techniques and the stabilization of Au clusters in solution or solid form allow us to investigate these subnanometric gold particles in different catalytic systems [30]. It is worth mentioning that, particle size is not only an important aspect for the reactivity but also is a

determining factor in the selectivity of certain catalytic reactions taking place on Au catalyst surfaces [30]. Molecular Au clusters have been demonstrated to be extremely sensitive towards the particular number of Au atoms present in the cluster. Thus, the reactivity of molecular Au-clusters can be fine-tuned by slight variations in the number of Au atoms in the small clusters [31]. Valden, Lai and Goodman have shown that the activity of Au nanoparticles deposited on TiO_2 is closely related to the electronic band gap of Au NP, where there exists a particular band gap (as well as a corresponding Au nanoparticle size of 2.9 nm) for the optimum catalytic activity towards CO oxidation [32]. On the other hand, a different study in the literature claimed that the binding of O_2 (which is the rate determining step for CO oxidation on Au catalysts) has less to do with the Au NP band gap but rather depends on the *'roughness'* or defect density of the binding site. This argument has been constructed on the fact that O_2 does not dissociate on the terraces of small Au clusters. Although such NP may have a proper band gap, dissociation can only occur on Au having coordinatively unsaturated Au atoms [33].

Previously, the activity of Au clusters was suggested to be simply due to under coordination, [34] however further studies revealed that reactivity was predominantly governed by the frontier orbitals (i.e. the highest occupied molecular orbital, HOMO or the lowest unoccupied molecular orbital, LUMO) and not by the coordination of the binding site.[35] To be more precise, the roughness (disorderness) of the surface orbital is responsible for the activity and not the geometric roughness. These frontier orbitals are mostly located at the under coordinated sites revealing a particular shape. There are reported examples in literature, where the reactivity trends in the literature clearly follow the nature of the frontier orbitals rather than the coordination/under coordination of Au NP [31].

Au nanoparticles consist of different facets e.g steps, kinks, terrace,(100) (111) and (110) etc. The behavior of these facets is different towards different reactions. Among these facets Au(111) is the most interesting, which has been used in the current studies that will be presented in the next chapters.

1.3.2 Surface Structure of Gold Single Crystals

Au crystallizes in a face centered cubic (fcc) structure, whose (111) termination undergoes reconstruction under UHV conditions [36]. Au surfaces, usually exhibit low Miller indece facets, i.e (100), (110) and (111) as shown in Figure 3. Planar surfaces such as Au(100), Au(110), Au(111), are relatively stable as they possess relatively low surface free energy of formation i.e. 0.08, 0.10, and 0.05 eV/A^2, where the coordination number of Au atoms on these surfaces are 7 for Au(100) [37], 11 for Au(110) [38], and 9 for Au(111) [39]. The lowest surface free energy of the Au (111) among the other surfaces is the reason behind the tendency of epitaxial Au thin films to expose (111) top facets [40].

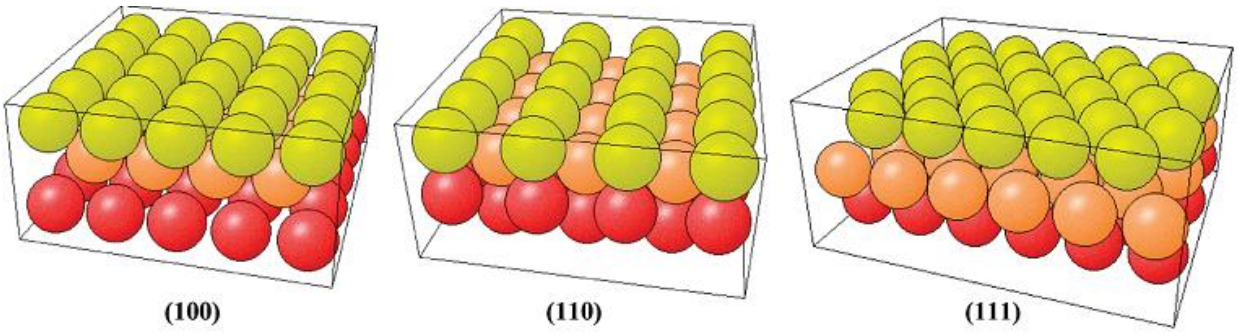

Figure 3. (100), (110), and (111) fcc crystal surfaces [permission requested from ref 41].

1.4 Surface Reconstruction

Au(111) surface experiences spontaneous reconstruction, so called the herringbone reconstruction, under UHV conditions as shown in Figure 5. The anisotropic environment of the surface atoms after the reconstruction changes the crystal symmetry both on the surface as well as in the near-surface (or sub-surface) region. These alterations in the symmetry and the displacement of surface atoms upon reconstruction decrease the surface free energy with respect to the perfect Au(111) surface in UHV. The exact nature and the mechanism of this transformation are still not fully known [42]. The surface atoms interact with vacuum on one

side and neighboring atoms on the other side. Hence, the surface atoms may alter their coordination number by slight positional relocation/relaxation that is associated with simultaneous change in their electronic structure [42]. The surface reconstruction of fcc metals can be also rationalized in terms of their distinctive surface states that arise due to the relativistic interaction of sp and d states [43]. This reconstruction on Au (111) affects the local reactivity of surface [44,36]. Scanning tunneling microscopy (STM) [45] and density functional theory (DFT) calculations confirmed the existence of the reconstruction of Au(111) in vacuum. The Au(111) surface has a 22 x √3 structure after the herringbone reconstruction (Figure 4) [46].

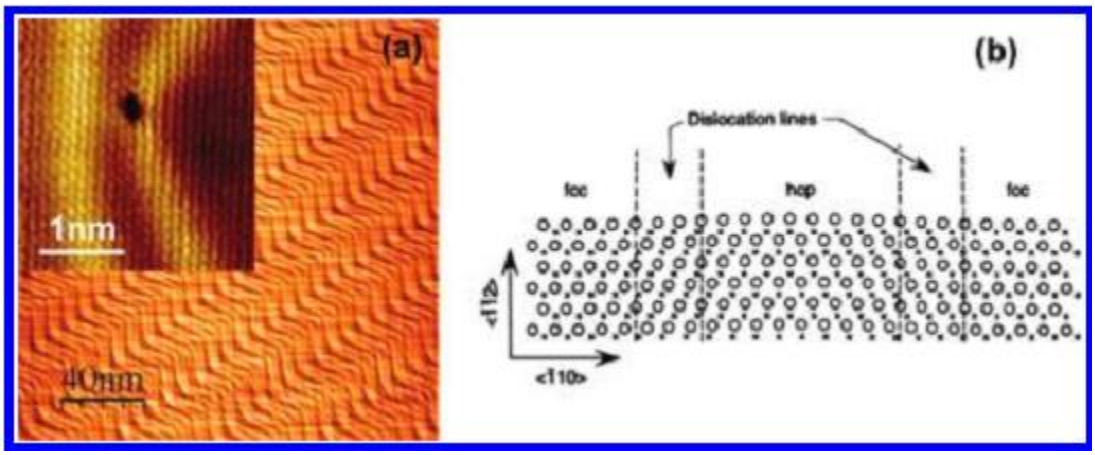

Figure 4 (a) STM image of the reconstructed Au (111) surface. (Inset) Atomic resolution of the edge dislocations (depressions) which are present at the elbows of the herringbone reconstruction. (b) In plane structure of the Au(111) reconstructed surface. The circle and crosses correspond to atoms in the first and second surface layers, respectively (Permission requested for reproduction from ref 46).

1.5 Adsorption of atoms/molecules on Au surface

As mentioned earlier, Au(111) is the most extensively studied single crystal gold surface both experimentally and computationally. Most molecules do not adsorb strongly on Au at room temperature. Vinod et al. showed that an insufficient number of steps on Au(310) limits any adsorption/desorption of H_2 under experimental conditions [47]. DFT calculations made by Okamoto showed that H_2 adsorption on Au (111) at the top of the cluster is an endothermic process (i.e.H atom adsorbed on atop sites is less stable compared to free H_2) while in the case of fcc and hcp hollow sites, H atom adsorption is slightly exothermic [48].

Koel's group reported that NO(g) practically does not adsorb on Au(111) at $T \geq 95$ K.[49] DFT studies of Yan and co-workers [50] also showed that NO adsorbs only weakly on Au(111). The dissociative adsorption of chlorine in a large temperature window on Au(111) with an activation energy of -8.7 kJ/mol was reported by Kastanas and Koel [51]. The adsorption of hydrogen sulfide and sulfur dioxide were found to be completely reversible on the Au(111) surface [52]. The SO_2 interaction is quite different among the other coinage metal surfaces, which can be attributed to the fact that their electronic properties (e.g poor electron donation from metal into the lowest unoccupied molecular orbital (LUMO) of SO_2 resulting in weak interaction) vary from metal to metal [52]. These examples clearly indicate the relatively low affinity of planar Au single crystal surfaces towards a variety of adsorbates which is in line with the inert nature of bulk Au systems which expose planar facets. However, adsorption of particular probe molecules can still yield very valuable information regarding the nature of the surface sites and the catalytic behavior of Au single crystal surfaces. Thus in the next few sections, a more detailed discussion on the adsorption properties of various relevant molecules on Au(111) single crystal model catalyst surfaces will be presented.

1.6 Adsorption of CO (Carbon Monoxide)

The surface structures of metallic single crystals have been investigated extensively via adsorption of probe molecules, particularly with CO. It is a well-established fact that the interaction of CO is very weak with Au, compared to other metals and the estimated energy for adsorption of CO on Au(111) surface at room temperature is of the order of c.a. 30 kJ/mol [56]. However, the CO adsorption on Au(111) surface can take place at cryogenic temperatures (e.g. 77 K) under UHV conditions. On the other hand, CO may strongly interact with Au(111) surface at high pressures [57]. Piccolo et al. studied the adsorption of CO via STM and polarization modulation reflection absorption infrared spectroscopy (PM-IRAS) and found that it can induce morphological changes on Au(111) [58]. When the Au(111) surface was subjected to CO exposure at room temperature and high pressure (10^{-3}-10^{3} Torr of CO), chemisorption takes place at under-coordinated sites, following the same classical trend in site-dependent adsorption energy (in terms of increasing adsorption strength): terraces < step < kinks < adatoms [58]. These results may be extended to other adsorbate systems and thus are important for elucidating the general reactivity trends of different adsorption sites on Au single crystal surfaces.

The CO interaction with the Au(110) surface was also studied by Outka and Madix at 125 K and it was found that no CO adsorption took place[59]. Gottfried et al. [60] investigated CO adsorption/desorption on Au(110) at lower temperatures and came up with five separate CO desorption states: α (multilayer at 32 K), β(second layer at 37 K), γ(physisorbed 1^{st} layer at 55 K), δ(Physisorbed 1^{st} layer at 67 K), and ε(chemisorbed at 145 K). The authors confirmed through ion bombardment experiments (which artificially produces surface defects) that the ε peak is associated with the regular surface of Au(110) and not from the defects [60]. The polarization resolved ultraviolet photoelectron spectroscopy confirmed that the chemisorbed CO on Au(110)[61] orients parallel to the surface revealing a unique adsorption geometry which is unlike Au(100) and Au(111) where CO binds to the surface through its oxygen end in a vertical fashion. Moreover, the CO adsorption on a Au (211) stepped surface has been investigated by

Kim et al. who found two adsorption states, α(from step site) and β (from terrace sites) [62]. RAIRS and TPD data allowed them to conclude that CO adsorbs strongly on the step sites (50 kJ/mol) compared to terraces sites (27-28 kJ/mol) [62].

These experiments clearly reveal the dissimilarities in the adsorption geometries of various adsorbates on different facets of Au surfaces under catalytic reaction conditions, which may be quite crucial for the understanding of catalytic reactivity and selectivity of Au catalysts in different reactions.

1.7 Adsorption of Hydrocarbons and Oxygenates

There is a general agreement that hydrocarbons and oxygenates molecularly (i.e. non-dissociatively) adsorb on clean Au single crystal surfaces and desorb in a reversible manner. In order to understand the hydrogenation and oxidation reactions in depth, it is paramount to understand the adsorption and desorption behavior of such molecules on Au single crystal surfaces. Hence in the coming sections, we will focus on the former studies in the literature on the adsorption and desorption properties of hydrocarbons and oxygenates on Au single crystal surfaces.

1.7.1 Hydrocarbons

The adsorption of ethylene and acetylene on Au(110) was studied by Outka and Madix, who reported that these two simple hydrocarbons did not decompose on the Au(110) surface [63,64]. Acetylene desorbs with a broad TPD peak between 125-200 K [63]. This broad peak reveals information regarding the nature of the weak chemisorption between these molecules and the surface, suggesting that these adsorbates have no well-defined binding sites on the Au(110) surface (i.e. no preferential adsorption sites). The desorption activation energy for acetylene is 42 kJ/mol. Ethylene desorbs with the similar TPD features without decomposing on the Au(110) surface [64,63].

Surprisingly, Davis and Goodman observed a very similar desorption behavior of propylene on Au(111) and Au(100) surfaces. The TPD spectra suggested that the molecular plane of propylene is slightly tilted towards the normal of the surface [65]. Propylene desorbs with two peaks: the monolayer desorbs at 140-145 K while the lower temperature peak is assigned to the multilayer which desorbs at 120 K. The small desorption activation energy (39 kJ/mol) is the evidence for the weak interaction of propylene with the surface [65]. The bonding energy of propylene with the Au surface was also calculated through DFT and suggests a very weak interaction in very good agreement with the TPD data [66].

Chesters and Somarjai observed the non-dissociative desorption of cyclohexene (c-C_6H_{10}), benzene (C_6H_6), and n-heptane (n-C_7H_{16}) on both Au(111) and stepped Au(766) surfaces.[64] On the other hand, naphthalene dissociates on both of these surfaces at room temperature[64].

The adsorption behavior of a series of n-alkane, 1-alkene and cyclic hydrocarbons on Au(111) has also been investigated by theoretical modeling. The physisorption energy for n-alkanes increases with increasing chain length by 6.2 kJ/mol per additional methylene unit[67,68]. Similarly, 1-alkenes also show a monotonic dependence of adsorption energy on chain length (with a slightly greater dependence than that of the corresponding alkanes).[67]

1.7.2 Adsorption/Desorption of Oxygenates on Single Crystal Au Surfaces

In the current work, we investigate the adsorption properties of various organic molecules on the Au(111) surface in relevance to their utilization in the partial oxidation reactions of alcohols. Therefore, providing a brief review of the existing literature on the oxygenate adsorption on Au single crystal surfaces would be in order.

Oxygenates including alcohols, aldehydes, ketones and epoxides weakly adsorb and desorb molecularly on clean Au(111), Au(110) and Au(100) surfaces [69,63,70,71,72]. For instance, one of the simplest alcohols such as methanol desorbs from the Au(111) surface with three desorption features: a monolayer desorption feature at 155 K and two different multilayer

desorption states corresponding to amorphous (143 K) and crystalline (134 K) domains[73]. Methanol can dissociate through breaking of the OH bond on the Au(310) surface containing surface defect sites (i.e. steps with (110) structure and terraces with (100) domains).[74] Molecular desorption of formaldehyde was observed with a broad peak at 160 K on Au(110). This broad peak can be explained using the weak interaction between the formaldehyde and the surface and the absence of a strongly specific site where it can differentially bind strongly [70]. Similarly, reversible adsorption of acetone occurs on Au(111) with desorption peaks at 160, 137, 132 K corresponding to monolayer, second layer and multilayer domains, respectively [75]. RAIRS studies indicated that acetone approaches the surface in a slightly tilted fashion through its oxygen end at low coverages. With an increase in the surface coverage of acetone, orientation of the adsorbate changes such that the C-O bond becomes parallel to the surface [75]. Outka and Madix studied the interaction of formic acid on the Au(110) surface with desorption peaks at 210 K (monolayer) and 175 K (multilayer). Dissociation of formic acid was also observed on the aforementioned stepped surface [70]. Chtaib et al. demonstrated the formation of formic acid anhydride as an intermediate on the Au(111) surface [76,77]. Ethylene oxide desorption occurs on the Au(211) surface with characteristic features at 115 K (multilayer), 140 K and 170 K from the monolayer. The peak at 140 K corresponds to the desorption from the terrace sites and 170 K from the step sites [78].

1.8 Oxygen Adsorption on Single Crystal Au Surfaces

In the partial oxidation reactions of alcohols, nature and the surface coverage of the oxidizing agent is one of the most crucial factors in the overall reaction mechanism. Thus in this section, we will very briefly summarize some of the crucial aspects that have been highlighted in the former studies in the literature regarding the delivery of oxidizing agents on Au single crystal surfaces.

Molecular oxygen (i.e. O_2) is arguably the most commonly used oxidizing agent in partial oxidation and total oxidation processes. In many typical catalytic oxidation processes, molecular oxygen is required to be activated/dissociated in order for the reaction to start/proceed. However, the dissociation probability of O_2 molecules is extremely low and typically below the

detection limit on the clean Au(111) surface within a broad range of temperatures and pressures [79]. Thus, activation of the Au(111) single crystal model catalyst surface in an oxidation process can only be made by the delivery of a particular oxidizing agents other than O_2, which can directly yield active atomic oxygen on the surface upon adsorption. Chemisorption of O_2(g) does not practically take place on Au(110) single crystals neither molecularly nor dissociatively above 100 K in UHV.[79] Although oxygen can physisorb on the Au single crystal surfaces at temperatures below 50 K, this physically/weakly adsorbed molecular oxygen cannot be converted into a chemisorbed state [79]. Chemisorption of oxygen on gold surfaces [80] has been mistakenly reported in the literature which has later been attributed to contaminations such as calcium[81] or silicon [82]. Oxygen sputtering and ozone decomposition methods have been utilized successfully in order to achieve atomic oxygen (O(ads)) delivery on the Au(111) surface [83,84]. DFT studies suggest that [85] upon ozone exposure of the Au(111) surface, generated atomic oxygen species prefer to bind onto the most stable FCC three fold hollow sites with a typical adsorption energy of E_{ad} = -3.08eV and the second most preferred adsorption site is the bridging site. Various probable adsorption sites of atomic oxygen (i.e. O(ads)) on the Au(111) surface as well as Au(111) surfaces containing different oxygen adatoms were depicted in Figure 6. The adsorption strength of atomic oxygen on these different probable adsorption sites can be ranked in the order of decreasing adsorption energy in the following manner: FCC hollow (3-fold site) > bridge (2-fold site) > HCP hollow (3-fold site) > atop [85].

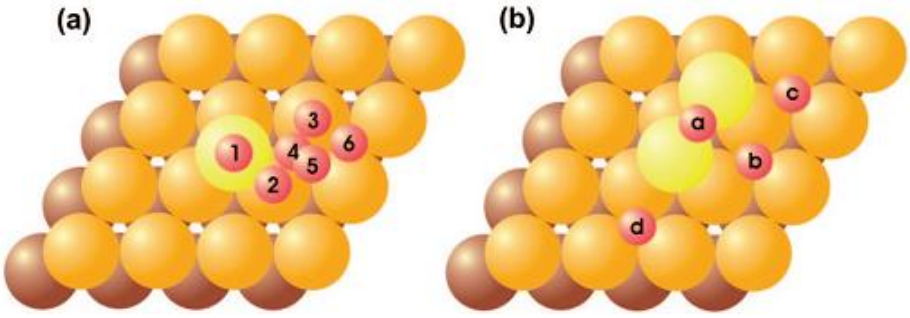

Figure 5. Adsorption of atomic oxygen on Au(111) at different sites containing one (a) or two (b) gold adatoms. Gold adatoms on the Au(111) surface are depicted with bright yellow color in the figure. [Permission requested from reproduction of ref 85]

1.9 Selective Oxidation of Oxygenates

After having discussed the literature on the adsorption properties of the individual reactants (i.e. hydrocarbons, oxygenates and adsorbed oxygen) on the Au (111) surface relevant to the partial oxidation and oxidative coupling processes; it is appropriate to summarize the existing literature on the co-adsorption and reaction of atomic oxygen with alcohols. When the Au(111) single crystal surface is properly activated [86] with adsorbed atomic oxygen, a broad range of selective oxidation reactions can be triggered [87]. One of the typical reactions that has been widely studied in the literature is the self-coupling of alcohols. Under proper experimental conditions, the self-coupling reaction of methanol on Au(111) surface can selectively yield an ester, a commercially valuable product (Figure 7) without any other partial/total oxidation products. The cycle of esterification *(*shown in Figure 7) is as follows. In the first stage, oxygen atoms are adsorbed on the Au surface which is followed by the adsorption of methanol. This adsorbed methanol species is activated by oxygen atoms present on the surface to form water and a methoxy group. The β-hydrogen is removed from the adsorbed methoxy species by the process called β-hydride elimination and ultimately results into the corresponding aldehyde. The methoxy species near by the aldehyde on the surface couple to form hemiacetal (note that the OH bond in the molecular hemiacetal is replaced by a O–Au bond). The second β-hydride elimination takes place and hemiacetal yields ester. The rate determining step for this reaction is the β-hydride elimination of the adsorbed alkoxy group to form the adsorbed aldehyde [63], as shown with the temperature programmed reaction spectroscopy (TPRS) by the observed primary kinetic isotopic effects [111]. Further interaction of aldehyde or ester with the adsorbed oxygen atoms on the surface yield the combustion products. Therefore the optimum concentration of oxygen should be kept at a low level during the partial oxidation and coupling reactions.

Figure 6. Mechanism for the self-coupling of methanol on O/Au(111). (Permission requested for reproduction from Ref 88).

Similarly, this mechanism can also be observed for the partial oxidation reaction of on the Au nanoparticles. Ideally, the highest coupling selectivity can be achieved, if the alkoxide of one co-adsorbed alcohol is isolated with aldehyde of another in order to form hemiacetal intermediate with two different alkyl groups. However in reality, the surface will be predominated by the alkoxy species, if the reactant mixture contains two different alcohols, then this will yield two self-coupled products and two cross-coupled products as depicted in Figure 8. However, if the β hydride elimination occurs much faster in one of the reactants as compared to the other one, then high selectivity can be obtained for one of the products. It should be noted that the concentration of alkoxide on the surface depends on the concentration of that particular species in the reactant gas mixture. These factors have been studied for methanol coupling with ethanol and 1-butanol on the oxygen pre-coverd O/Au(111) surface [111,112]. The stability of alkoxy species on the surface for different alcohols decreases in the following order: butoxy > ethoxy > methoxy. Therefore ethanol will displace methanol to form ethoxy and will reform methanol. The rate constant for β-hydride elimination to form the corresponding aldehyde decreases with a similar order i.e butoxy > ethoxy > methoxy. It has also been confirmed through computational studies that β hydride elimination is a slow step which is promoted by

adsorbed O or CH_3O [113]. The general mechanism shown in Figure 7 associated with the self-coupling of alcohols on O/Au(111) also serves as a guiding mechanism for other similar oxidative coupling reactions. Probably one of the most important revelations of this mechanism is the fact that the reaction involves a nucleophilic attack by the methoxy group on the electropositive carbon of the formaldehyde which is produced as an intermediate [88].

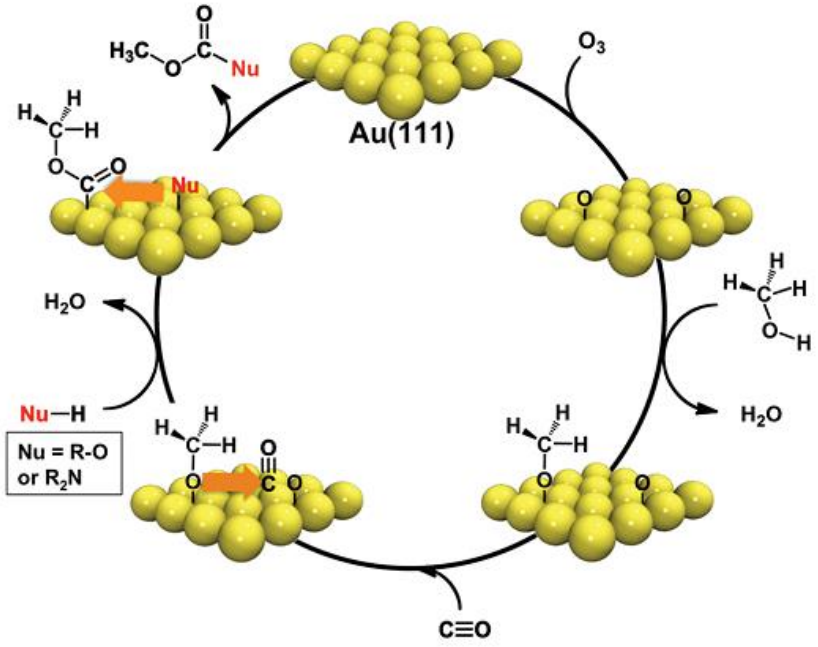

Figure 7. A general reaction mechanism for the gold-mediated carbonylation/oxidative coupling of methanol using a generic nucleophile.(Permission requested from ref 89)

Figure 7 demonstrates that the general reaction mechanism of the methanol self-coupling process can be used as a springboard to design a large variety of novel oxidative coupling reactions with the help of alternative nucleophiles (e.g. R_2N). For instance, in the mechanism shown in Figure 7, carbonylation of methanol competes with the self-coupling of methanol due to the presence of CO in the reaction medium. Thus, a variety of novel catalytic products can be obtained. These two different reaction pathways (self-coupling versus carbonylation) are summarized in Figure 8 [89].

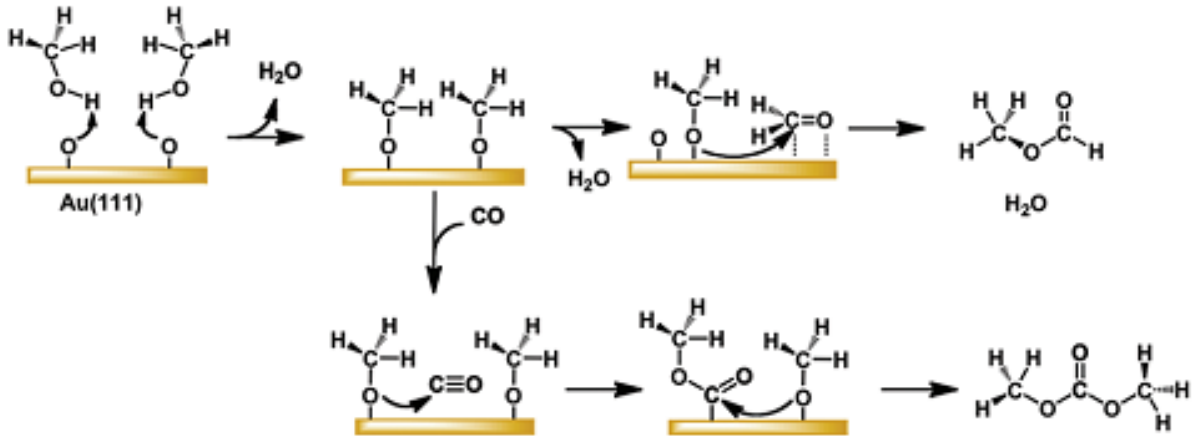

Figure 8. Pathways for competing coupling reactions. Oxidative self-coupling of methanol to methyl formate (upper) and coupling to CO yielding dimethylcarbonate.(Permission requested from ref 89)

The cross coupling reaction of methanol with acetaldehyde, benzaldehyde and benzene acetaldehyde gives methylacetate, methyl benzoate, and benzene acetic acid methyl ester, respectively [90]. A similar cross coupling reaction occurs between dimethylamide and aldehyde (formaldehyde, acetaldehyde, propanal, and butanal) forming the corresponding amides [91]. Friend et al. studied the partial oxidation of trans-b-methylstyrene, a-methylstyrene and allylbenzene (three isomers of phenyl-substituted propene) to show the effect of geometry and acidity of the respective compounds in the gas phase on the products. They concluded that trans-b-methylstyrene, and a-methylstyrene on reaction at O/Au(111) form the epoxide because it is slightly acidic compared to allylbenzene (highly acidic), where no epoxide formation occurs [92]. Propene is often used to understand the reaction mechanism for allylic oxidation. Complete combustion of propene occurs on Ag(110) [93,94] and Ag(111) [95] while on Au(111), it partially oxidizes to acrolein, acrylic acid, and carbon suboxide due to C-H activation [96]. The Au(111) surface is good at selective oxidation, yet many reactions can go to total combustion even on Au surfaces. The concentration of oxygen is one of the few factors dictating the extent of oxidation. Total oxidation is favored for high surface atomic oxygen coverages [97].

1. EXPERIMENTAL

2.1 Ultra-High Vacuum Experimental Set-up

In surface science experiments, in order to avoid any ambiguity the surface needs to be atomically well-defined and the composition of the top most layer should remain constant. This means that the concentration of molecules or atoms originating from the gas phase must be kept low. Validity of this requirement can be readily evaluated from the simple kinetic theory of gases. The flux of atoms or molecules in vacuum can be expressed as: [99]

$$r = 3.51 \times 10^{22} P / (TM)^{1/2} \qquad (1)$$

where *P* is the pressure (in *Torr)*, *T* is the Kelvin temperature and M is the molecular weight in atomic mass units and the flux, *"r",* is given in molecules $cm^{-2}s^{-1}$. For instance, N_2 molecules (M=28) at room temperature (T=298 K) at 1 Torr have an arrival rate of 3.88×10^{20} molecules $cm^{-2}s^{-1}$.

This interaction can be reduced by using a vacuum chamber with a reduced pressure which will increase the mean free path of the molecules or atoms and as a result the molecule or atoms will mostly interact with the walls of the chamber [100]. The vacuum level in a given experimental system is conventionally categorized as described in *Table 1*.

Degree of Vacuum	***Pressure Range***
Low	1000-1 mbar
Medium	$1\text{-}10^{-3}$ mbar
High	$10^{-3}\text{-}10^{-7}$ mbar
Ultra-High	$10^{-7}\text{-}10^{-14}$ mbar

Table 1. Pressure ranges for vacuum technologies.

In the current work, all of the experiments were performed in a multi-technique UHV surface analysis chamber (Figure 9) with a base pressure of 2.0 x 10^{-10} Torr. In order to maintain the base pressure, three dual-stage rotary vane pumps (RVP), one turbo molecular pump (TMP) and one titanium sublimation pump (TSP) were utilized. The pressure in the UHV chamber was measured by a Bayard-Alpert type ionization (ion) gauge (1.0 x 10^{-3} - 5.0 x 10^{-11} Torr and a thermocouple (TC) gauge (1.0 x 10^{-3} – 760 Torr), while the pressure of the gas manifold was measured by a capacitance manometer (1 - 760 Torr) and a TC gauge (1.0 x 10^{-3} – 760 Torr). The UHV chamber is equipped with an Al/Mg K_α dual anode X-ray source and a double-pass cylindrical mirror analyzer (CMA) for XPS, a reverse-view Low Energy Electron Diffraction (LEED) optics, and a quadruple mass spectrometer (QMS) for TPD and residual gas analysis (RGA). An atomically polished double-sided Au (111) single crystal (10 mm diameter, 2 mm thickness from MaTeck GmbH) was used as a substrate. The single crystal was mounted on a tantalum sample holder and assembled to a high-precision manipulator. The sample temperature was monitored by a K-Type thermocouple which was spot-welded on the peripheral edge of the crystal. The clean Au(111) was obtained by multiple cycles of Ar^+ sputtering at 1.5 kV at room temperature (RT) and subsequent heating to 770 K in vacuum. An utmost effort has been spent in order to avoid over heating of the Au single crystal surface which has a relatively low melting point of 1337 K at 1 atm.

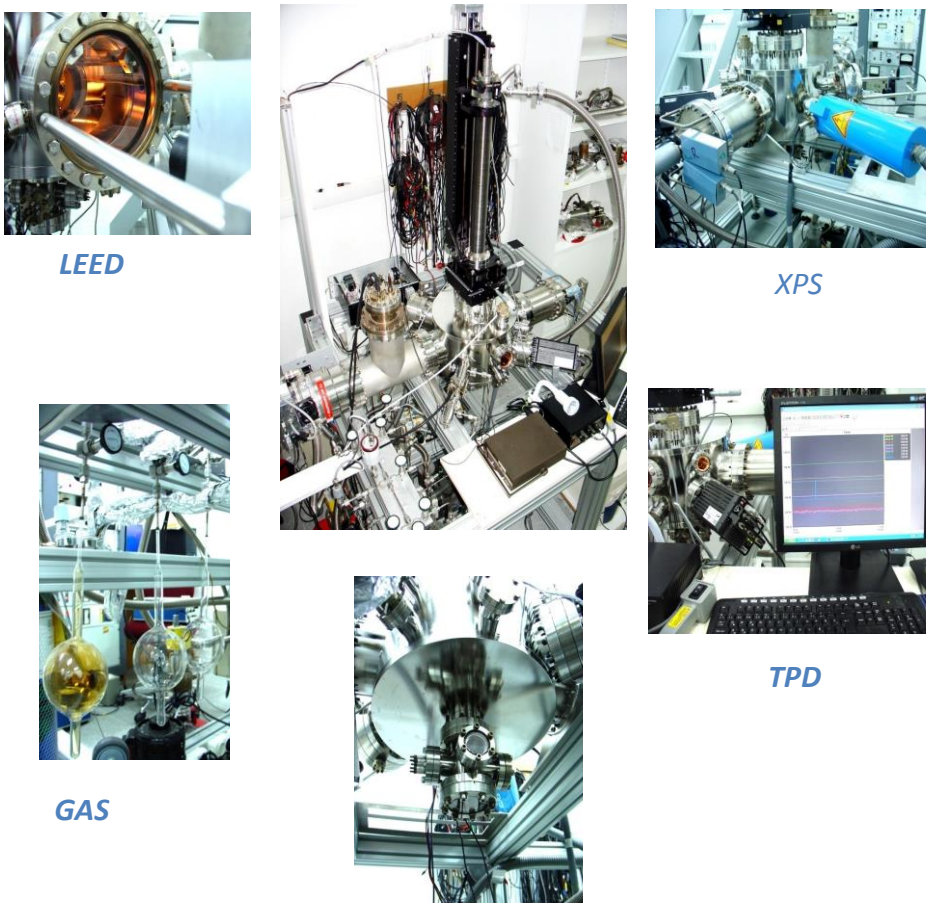

Figure 9. The visual representations of multi-technique UHV surface analysis chamber.

2.2.1 Sputtering Ion Gun (LK Technologies NGI3000 Sputtering Gun)

Sputtering is the removal of surface atoms with energetic particle bombardment. It is caused by the collisions between the incoming particles (i.e. ions) and the atoms in the near surface layers of a solid [101]. Generally, an incoming particle collides with the atoms of the solid, transferring energy to the atomic nuclei. A surface atom becomes sputtered if the energy transferred to it has a component normal to the surface which is larger than the surface binding energy. This is usually approximated by the heat of sublimation which is mostly smaller than the displacement

energy necessary to create a stable dislocation. The LK Technologies Model NGI3000 Ion Gun with control electronics is designed for the cleaning of surfaces by noble gas ion sputtering with beam energies up to 3 keV and ion currents up to 25 μA. In the current UHV system, ultra high purity Ar gas (> 99.9999, Linde GmbH) is used for sputtering. The gun employs a noble gas injection system which allows sputtering to take place at a typical Ar (g) pressure of 1 x 10^{-6} Torr. In this system, the gas to be ionized by electron impact ionization is injected directly into an enclosed ionization region which houses a thoria coated iridum filament and a grid structure. The ion beam is then accelerated out of the ionization chamber to the target. The gun also contains an integral high-precision leak valve to supply a source of noble gas (i.e. Ar).

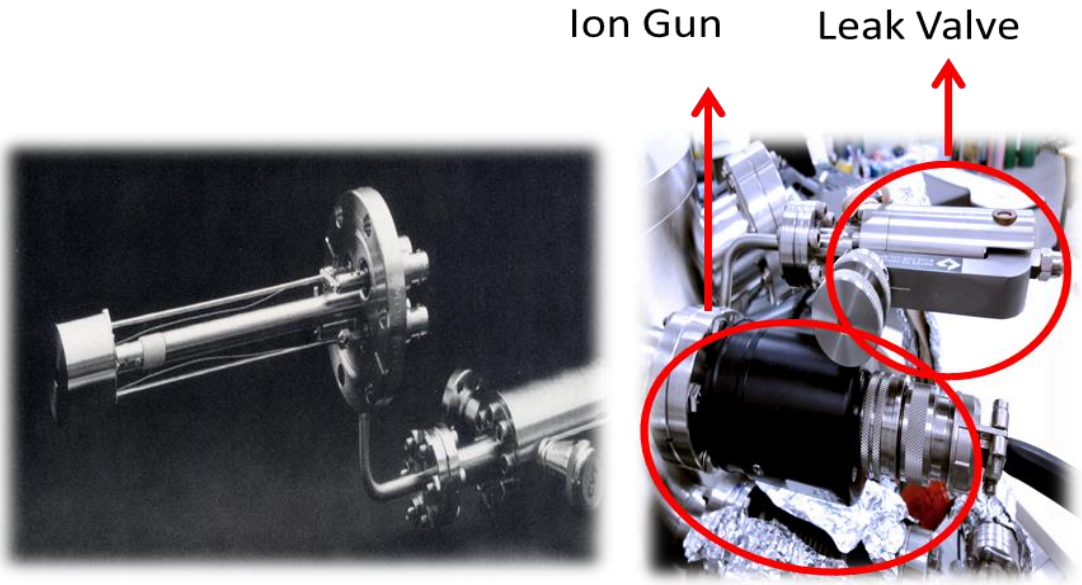

Figure 10. LK technologies sputtering ion gun with a high-precision leak valve

The NGI3000 has variable beam accelerating voltage (0.2 to 3 kV). The sputtering ion beam diameter depends on the length between the ion gun and target. Typical distances from the gun end to the target are 5-15 cm. The beam has a gaussian shape and a 3 cm diameter at 14 cm gun to target distance. The gun doesn't need a differential pumping stage and the nominal source pressure is typically 5 x 10^{-5} Torr when the nominal chamber pressure is 1 x 10^{-6} Torr. For initial operation or after exposure to atmosphere, the ion gun should be degassed by operating the gun under high vacuum at 20 mA for a period of 30 minutes.

2.2.3 Temperature Controller (Heat Wave Labs Model 101303-46A)

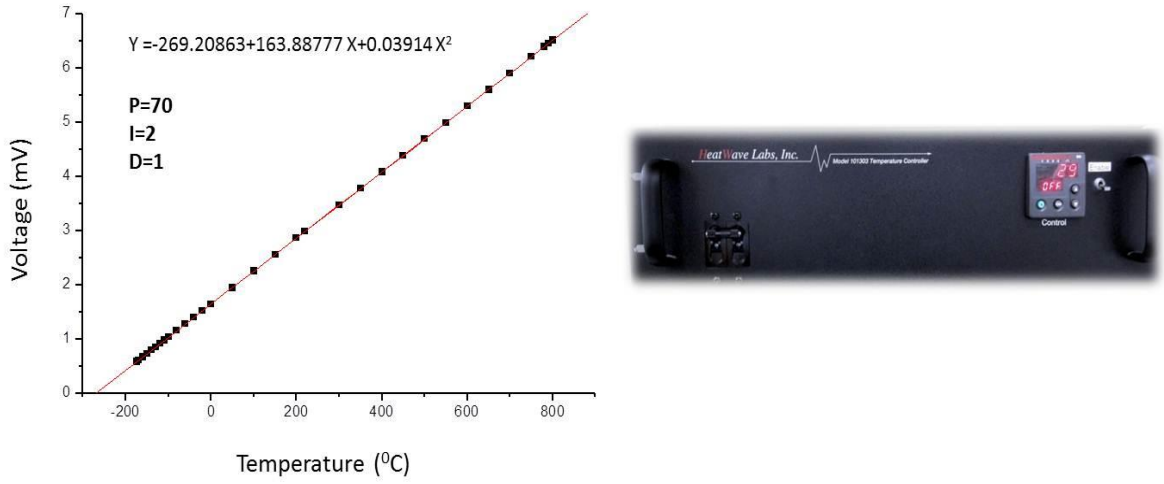

Figure 11. Sample temperature controller unit used in UHV chamber.

The sample temperature was manipulated with an electronic temperature controller (Heat Wave Labs Model 101303-46A). The sample temperature is measured with a K-type thermocouple. Type K thermocouple consists of chromel (90% nickel + 10% chromium with 0.05 mm thickness), alumel (95% nickel + 2% manganese + 2% aluminum + 1% silicon with 0.05 mm thickness) alloys. It can be used for the temperature interval of 20 K and 1600 K. Our working temperature interval was between 80 K to 800 K. After several optimization tests, PID parameters for a linear heating protocol were determined in order to obtain a linear heating ramp. The following parameters were used in the PID algorithms during the linear sample heating ramps: P=70, I=2, D=1. The first parameter, *proportional control* (P), depends only on the difference between the set point and the process variable. This difference is referred to as the "error term". Therefore, proportional control determines the ratio of output response to the error signal. When the value is in the band, the controller adjusts the output based on how close the process value is to the set point. The second parameter, *integral* (I), determines the speed of correction. The integral component sums the error term over time. A low integral value causes a fast integration action. The last parameter, *derivative* (D), is used to minimize the overshoot in a PI-controlled system. It adjusts the output based on the rate of change in the

temperature or process value. If the derivative value is too high, then the system becomes sluggish. In all of the current experiments, a resistive linear heating rate of 1 K/s was chosen and all the system parameters were optimized according to this linear ramp rate.

2.3 Surface Analytical Techniques

2.3.1 Low Energy Electron Diffraction (LEED)

Low-energy electrons with energies varying from 20 to 500 eV are ideal probes for surface science studies because they are easily scattered by atoms both elastically and inelastically. [102] If they penetrate into a solid for more than four or five atomic layers they are absorbed and disappear into the electron sea, however, if they survive absorption in the first two or three atomic layers and back-scattered out of the crystal, they can provide information about the atomic arrangement in the surface layer.

Consider the reflection of two parallel electrons of the same wavelength by two adjacent planes of a lattice as shown in Figure 12.

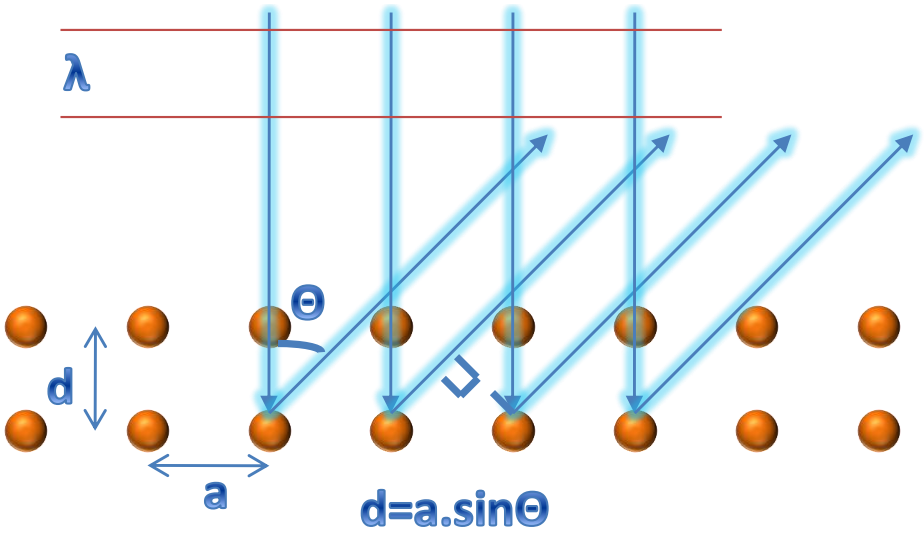

Figure 12. Bragg's diffraction condition (adapted from ref.103).

where θ is the glancing angle. For many glancing angles the path-length difference is not an integer number of wavelengths, and the beams interfere destructively. However, when the path-length difference is an integer number of wavelengths, the reflected beams are in phase and interfere constructively. This is explained by Bragg's law:[103]

$$n \lambda = 2d \sin\theta \qquad (2)$$

Reflections with n = 2, 3, ... are called second order, third-order and they correspond to path-length differences of 2, 3, ... wavelengths. Bragg's law is used in the determination of the spacing between the layers in the lattice. Once the angle θ corresponding to a reflection has been known, d can be calculated.

LEED experiments are performed with a narrow beam of electrons with energy between 20 eV and 500 eV. They must be incident on a planar single crystal surface at a given angle. The sample surface must be well-oriented, electrically grounded, planar and either clean or contaminated in a controllable manner. An experiment for surface structure analysis consists of three main parts: the electron gun to generate the incident electron beam, a manipulator to hold and orient the sample and a detector to monitor the diffracted beams.

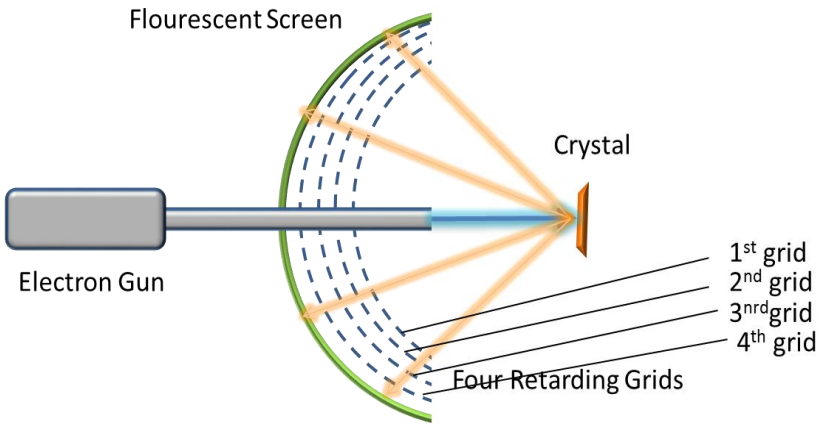

Figure 13. Schematic representation of a Low Energy Electron Diffraction experiment.[104]

Electrons are generated either by on-axis indirectly heated cathodes or by off-axis tungsten filaments, with energies that can differ between 0 and 800 eV. The effective diameter of the electron beam is about 1 mm [102] for the display system where the retarding-field energy analyzer is used. It consists of four hemispherical concentric grids and a fluorescent screen as shown in *Figure 15* [104]. The first grid is connected to the earth ground to provide a field-free region between the sample and the first grid. This reduces an undesirable electrostatic deflection of diffracted electrons. A negative potential is applied to the second and third grids (suppressor grids) to allow the transmission of the elastically scattered electron to the fluorescent screen in a narrow range. The fourth grid is usually grounded to reduce field penetration of the suppressor grids by the screen voltage when a potential of a few kilovolts (typically 2 keV) is applied to the screen in order to make the diffraction beams visible.

In order to consider the symmetry of a perfectly ordered surface, there are two parameters that must be known, lattice and basis. The lattice consists of a two-dimensional array of points which possess translational symmetry [104]. The basis, on the other hand, represents the arrangement of the atoms with respect to the lattice points of the surface, for

instance it specifies all atomic positions within one unit cell. The five different surface lattices and their diffractions in the LEED experiments are shown in *figure 14*:

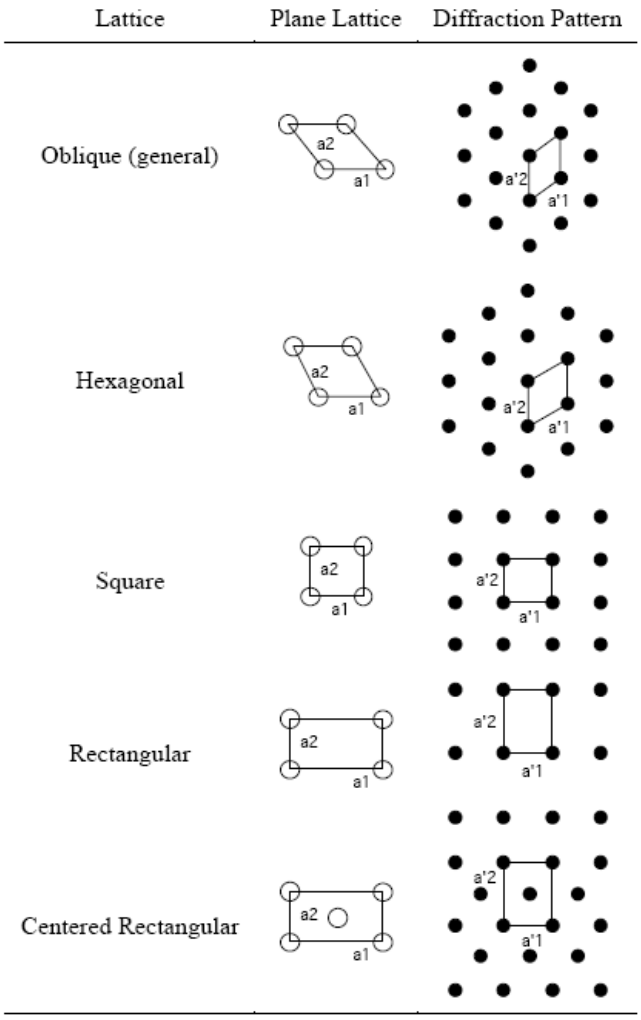

Figure 14. Diffraction patterns of five plane lattices. [ref. 104]

A two-dimensional solid surface contains a primitive unit cell which is defined by the translational vectors $\overrightarrow{a_1}$ and $\overrightarrow{a_2}$. These vectors can be defined in Cartesian coordinates $\hat{x}$ and $\hat{y}$, the unit cell of the surface can be described by the matrix **A**, the elements A_{ij} of which are related to the translational vectors:

$\overrightarrow{a_1} = A_{11}\hat{x} + A_{12}\hat{y}$ (3)

$\overrightarrow{a_2} = A_{21}\hat{x} + A_{22}\hat{y}$ (4)

Associated with the (real space), the two dimensional unit cell in reciprocal space can be described by a matrix $\mathbf{A}^*$.

The relationships between the primitive translation vectors of the surface, $\overrightarrow{a_1}$ and $\overrightarrow{a_2}$ and the primitive translation vectors of the reciprocal lattice, $\overrightarrow{a_1}^*$ and $\overrightarrow{a_2}^*$ can be written as

$$\overrightarrow{a_1}^* = 2\pi \left[\frac{\overrightarrow{a_2} \, x \, \overrightarrow{n}}{\overrightarrow{a_1}.(\overrightarrow{a_2} \, x \, \overrightarrow{n})}\right] \quad (5)$$

$$\overrightarrow{a_2}^* = 2\pi \left[\frac{\overrightarrow{n} \, x \, \overrightarrow{a_1}}{\overrightarrow{a_2}.(\overrightarrow{n} \, x \, \overrightarrow{a_1})}\right] \quad (6)$$

when $\overrightarrow{n}$ is taken to be a unit vector normal to the surface.

If a surface lattice is characterized by two base vectors a_1 and a_2, the reciprocal lattice follows from the definition of the reciprocal lattice vectors a_1^* and a_2^*:[105]

$$\overrightarrow{a_i}.\overrightarrow{a_j}^* = \delta_{ij} \quad (7)$$

where δ_{ij} is the Kronecker delta, $\delta_{11} = \delta_{22} = 1$, $\delta_{12} = \delta_{21} = 0$. (The dot product is equal to $|\overrightarrow{a_i} \times \overrightarrow{a_j}^*|\cos\alpha$) Therefore, when $\overrightarrow{a_1}$ and $\overrightarrow{a_1}^*$ parallel:

$\overrightarrow{a_1} . \overrightarrow{a_1}^* = 1$ (8)

$|\overrightarrow{a_1} \times \overrightarrow{a_1}^*|\cos\alpha = 1$ (9)

$|\overrightarrow{a_1}| = 1/ |\overrightarrow{a_1}^*|$ (10)

For instance, for an fcc (111) surface;

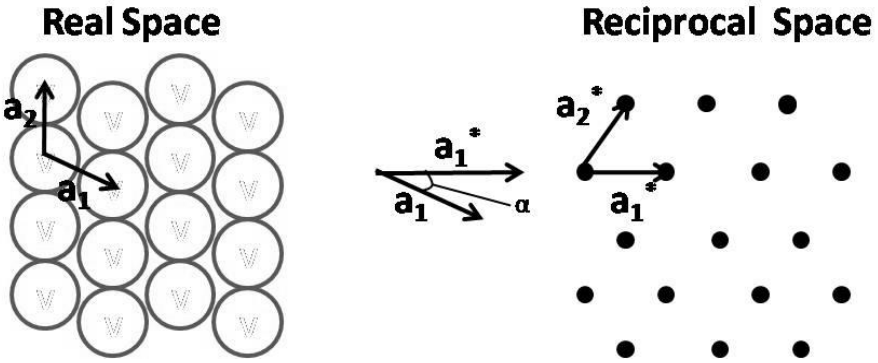

$\mathbf{a_1}^*$ is not perpendicular to $\mathbf{a_1}$ and $\mathbf{a_2}^*$ is not perpendicular to $\mathbf{a_2}$, $\alpha = 30^0$, $\cos\alpha = \sqrt{3}/2$,

$$a_1^* . a_1 = 1 \quad (11)$$

$$| a_1^* \times a_1 | \cos\alpha = 1 \quad (12)$$

$$| a_1^* \times a_1 | \sqrt{3}/2 = 1 \quad (13)$$

$$| a_1 | = 2/\sqrt{3} . (1/a_1^*) \quad (14)$$

Overlayer surface structures may have lattice vectors $\mathbf{b_1}$ and $\mathbf{b_2}$ which differ from the substrate lattice vectors $\mathbf{a_1}$ and $\mathbf{a_2}$. However they can be described in terms of the substrate lattice vectors as follows: [106]

$$b_1 = m_{11}a_1 + m_{12}a_2 \quad (15)$$

$$b_2 = m_{21}a_1 + m_{22}a_2 \quad (16)$$

which can be expressed in matrix notation as:

$$\begin{pmatrix} b_1 \\ b_2 \end{pmatrix} = \begin{pmatrix} m_{11} & m_{12} \\ m_{21} & m_{22} \end{pmatrix} \begin{pmatrix} a_1 \\ a_2 \end{pmatrix} \quad (17)$$

or

$$b = M.a \quad (18)$$

A corresponding relationship between reciprocal lattice vectors may be similarly defined as:

$$b^* = M^* . a^* \quad (19)$$

where

$$M^* = \begin{pmatrix} m_{11}^* & m_{12}^* \\ m_{21}^* & m_{22}^* \end{pmatrix} \quad (20)$$

with a standard matrix algebraic operation, one can relate these matrices as follows:

$$\begin{pmatrix} m_{11} & m_{12} \\ m_{21} & m_{22} \end{pmatrix} = 1/\det M^* \begin{pmatrix} m_{22}^* & -m_{21}^* \\ -m_{12}^* & m_{11}^* \end{pmatrix} \quad (21)$$

where

$$\det M^* = m_{11}^* . m_{22}^* - m_{21}^* . m_{12}^* \quad (22)$$

This relationship is enough to present the real space structure to be derived from the observed diffraction pattern if the appropriate reciprocal lattice vectors are extracted from the pattern observed.

2.3.2 Temperature-Programmed Desorption (TPD)

TPD is a useful technique in surface science, where the desorption of gases from single crystals or polycrystalline materials into the vacuum is examined as a function of desorption temperature [107]. Figure 15 shows a typical schematic set-up for TPD.

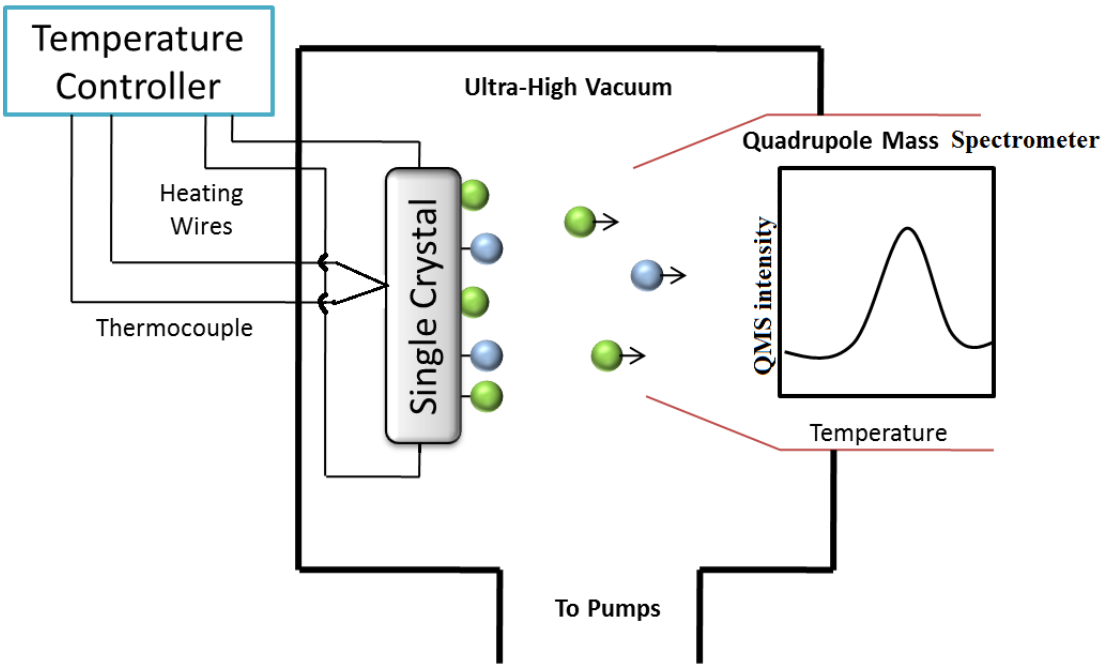

Figure 15. Experimental set up for Temperature Programmed Desorption (TPD) technique in ultra-high vacuum. (adapted from ref [105].

The single crystal mounted on a manipulator in a UHV chamber is heated resistively via copper wires. In order to monitor the temperature, a thermocouple which is spot-welded to the back of the crystal is used. Heating rates employed in TPD can vary from 0.7 to 70 K.s $^{-1}$, but the usual range is between 1-5 Ks^{-1} (in our experiments, this value is chosen to be 1 Ks^{-1}) [108]. The quadruple mass spectrometer is utilized in order to measure the types and concentrations of the desorbing species.

The dependence of the rate of evolution of adsorbed molecules from a surface, on the temperature, is given by the general Arrhenius equation [108].

$$-\frac{dN}{dt} = k_m N^m \exp(-E_d/RT) \qquad (23)$$

N is the surface concentration of adsorbed particles per unit area, k_m is the frequency factor, m is order of the desorption reaction, E_d is the activation energy of the desorption

process and T is the absolute temperature. For m=0, i.e. for a zero order desorption kinetics, adsorbates are relatively weakly bound to the surface in the presence of a practically infinite adsorbate reservoir which is typically valid for multi-layer desorption states. For m=1, i.e. for a first order desorption kinetics, the particles desorb almost independent of each other. For m=2, i.e. for a second order desorption kinetics, the particles must combine before desorption where their recombination is rate-determining.

TPD can provide information about the adsorbate coverage, adsorption energy (which is comparable to the activation energy of desorption), lateral interactions between the adsorbates, coverage dependence of the adsorption energy and the pre-exponential factor of desorption.

The basic experiment involves adsorption of one or more species on the sample surface at a given temperature and heating of the sample in a controlled manner while monitoring the evolution of species from the surface back into the gas phase. The data obtained from such an experiment consists of the intensity variation of each recorded mass fragment as a function of temperature. The area under a peak is proportional to the amount of the adsorbed species. The kinetics of desorption gives information about the aggregation of adsorbed species i.e. molecular vs. dissociative. The position of the peak is related to the enthalpy of adsorption i.e. to the strength of binding to the surface. The desorption behavior of molecules from the surface is quite different, they may desorb in a zero order, 1^{st} order and 2^{nd} order fashion. Before going into further detail, we can look at a few general aspects of different desorption kinetics observed in TPD experiments.

a. Zero-order desorption kinetics

This type of desorption (depicted in Figure 16) occurs in multilayers when the reservoir of the desorbing molecule is infinite. It can also be observed if the interaction between the adsorbates is very strong, exceeding the weak interaction between the adsorbate and the surface. The desorption rate in zero order kinetics does not depend on the adsorbate coverage while the desorption signal maximum strongly depends on coverage. It means that the desorption temeparture increases exponentially with temperature. The finger print of zero-order

desorption is that all peaks have the common leading edge. There is a sharp decline in the desorption intensity immediately after the desorption maximum. The desorption peak shifts towards a high temperature monotonically, with an increase in the adsorbate coverage [109].

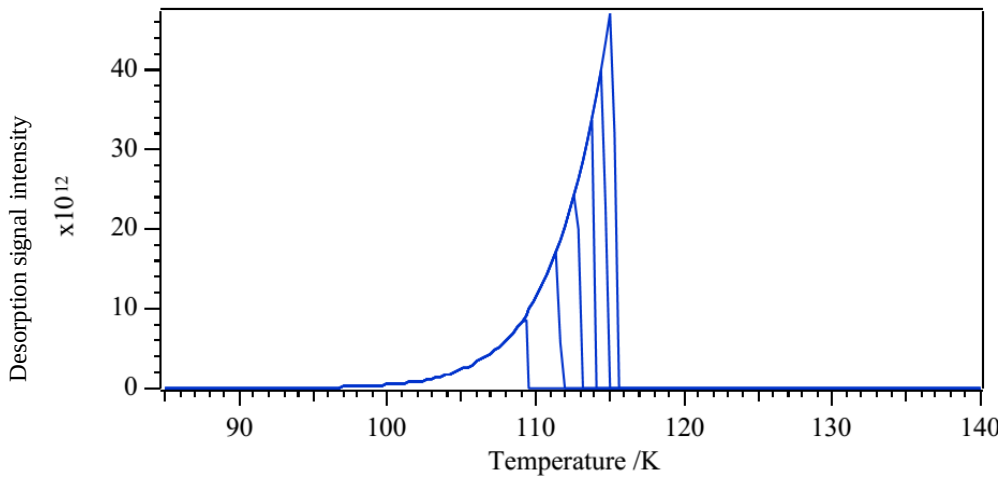

Figure 16. Zeroth order desorption kinetics. [Permission requested for reproduction from ref 109]

b. First order desorption kinetics

1st-order desorption behavior is shown in Figure 17. The rate of desorption is directly proportional to the coverage of the adsorbate. The temperature remains constant with increasing coverage, because the interaction between adsorbate and the surface remains almost constant despite that there is an increase in the coverage, as interaction between adsorbate and surface is already large in the first monolayer. The desorption maximum temperature is closely related to the desorption energy of the adsorbate with respect to the surface [109].

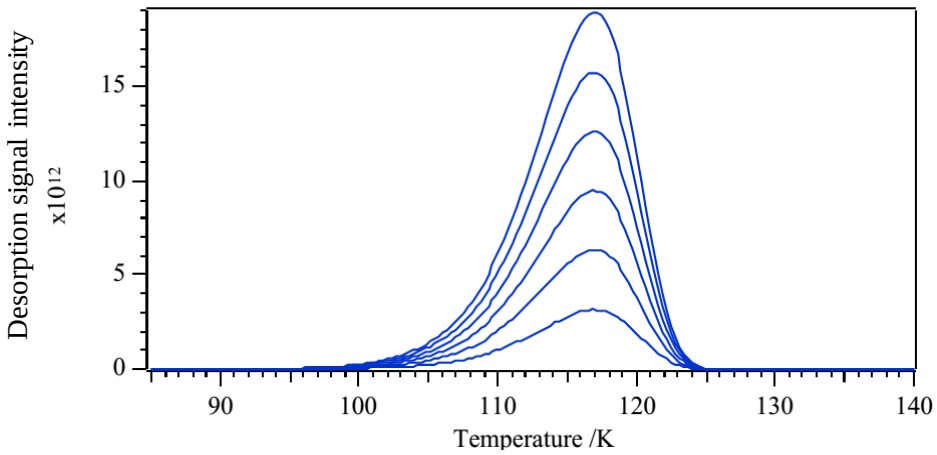

Figure 17. First-order desorption kinetics [Permission requested for reproduction from ref 109]

c. Second-order desorption kinetics

Second-order desorption (shown in the Figure 18) is only observed when molecules desorb in a recombinative fashion. The rate of desorption is directly proportional to the square of coverage. Thus, the desorption maximum shifts to lower temperatures with increasing adsorbate coverage facilitating easier recombination and desorption. The shape of the desorption signal is characteristically symmetric with a common trailing edge for all adsorbate coverages [109].

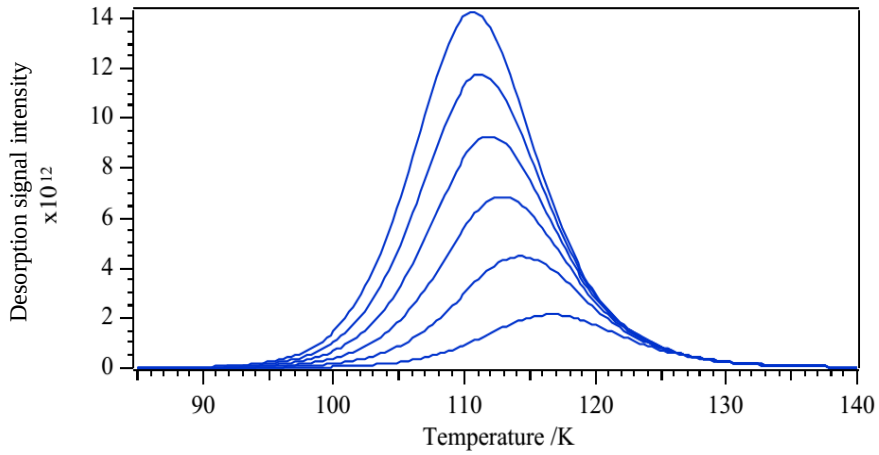

Figure 18. Second-order desorption kinetics [Permission requested from ref 109].

2.3.3 Redhead Analysis

Theoretical models of TPD are very helpful in understanding the TPD spectra and estimating the thermodynamic and kinetic parameters. Redhead method is often used to determine the activation energy for a first-order desorption process [110]. The determination of desorption energy requires the estimation of the value of pre-exponential factor "v". A value of 10^{13} s^{-1}" is commonly used for v. The remaining term "$\ln(E_{des}/RT_{max})$" is a small value and is typically estimated to be 3.64.

$$\Delta \boldsymbol{E}des = R\boldsymbol{T}max\left[\ln\frac{\nu 1.\boldsymbol{T}max}{\beta} - \ln\frac{\Delta \boldsymbol{E}des}{R\boldsymbol{T}max}\right] \quad (24)$$

There is a relatively straight forward relation between E_{des}, v and T_{max}. Redhead model assumes that the activation parameters do not depend on the coverage of the adsorbate and desorption process exclusively follows 1st order kinetics [110].

2.4 Sample Preparation

2.4.1 Sputtering of the Sample

In order to remove various types of surface contaminations and/or clean the carbonaceous species such as (graphitic/carbidic carbon or carbonates) from the Au(111) single crystal surface, highly energetic Ar^+ ions were emitted towards the surface. For ion bombardment with an oblique angle of incidence, the sputtering yield increases with increasing the angle of incidence up to 70^0. In order to monitor the ion current between the sample and the sputter ion gun, Keithley 197 model digital multimeter in the μA reading mode was connected to the sample via one of the copper heating legs while the other multimeter connection was electrically grounded. Then, inert argon gas was sent into UHV chamber through a leak valve and the pressure of the UHV chamber was stabilized at $1x10^{-6}$ Torr. An important point is that the beam emission must be applied after adjusting the Ar^+ pressure

otherwise a discharging might occur in the inner walls of the sputter ion gun. For the energy of the ion beam, the emission with a value of 15 mA and the beam voltage with a value of 1.5 kV have been used during the sputtering procedure. The beam voltage and the emission values must be increased slowly and consecutively. Higher emission and beam voltage values can decrease the sputtering yield since highly energetic Ar^+ ions which can penetrate into single crystal can damage the substrate surface by removing atoms from the top layers of the substrate. Using these sputtering parameters, a typical ion beam current of 10 – 18 μA can readily be achieved during the etching process.

2.4.2. TPD Experimental Procedure:

These experiments were performed using the following stepwise procedure:

1. The manifold, leak valves, manipulator and UHV chamber was baked at 110 °C for >48 h to desorb the molecules from the walls of the chamber in order to avoid any contamination during the experiment. This baking process also improves the base of the UHV system during the TPD experiments. Note that the optimum pressure required for the TPD experiments is < 5 x 10^{-10} Torr. Turbo molecular pump, titanium sublimation pump and a scroll pump is used to reach the required pressure.

2. QMS is outgassed (for >12 h) by turning on the filament and multiplier and applying 70 eV ionization voltage and 2000 V multiplier voltage simultaneously.

3. The ultra-high purity organic chemicals that will be used in the TPD experiments as adsorbates are further purified in the manifold via freeze-thaw-pump cycles, using liquid N_2 traps.

4. The Au(111) single crystal was mounted on the tantalum wires and cooled with liquid N_2 down to c.a. 90 K (because adsorption of oxygenates do not occur at higher temperatures on the Au(111) single crystal surface).

5. The Au(111) single crystal surface was cleaned from the contaminants by sputtering the surface with Ar ions, while keeping the sample in front of the Ar ion gun for 5-10 minutes. The beam current should be checked regularly during sputtering with the help of pico-ammeter. The beam current usually ranges within 5-10 μA.

6. The sputtering leads to a slightly defective surface. Thus, in order to heal the surface defects, the sample was annealed from 90 K to 750 K.

7. Next, the sample was cooled back to 90 - 100 K and the organic compound under investigation was dosed through a leak valve onto the sample while keeping the Au(111) crystal in front of the tubular doser (with a 10 mm outer diameter, matching the sample diameter) which was mounted on a linear UHV transition/motion stage.

8. The sample with the adsorbed organic compound was moved in front of the mass spectrometer with the help of the manipulator (through X,Y,Z,θ motion). Then, QMS was set to record various desorption channels with a 50ms dwelling time per channel. These desorption channels were chosen based on the mass spectroscopic fragmentation patterns of the reactants as well as the expected desorption products. NIST mass spectroscopy database [122] was used for determining the most intense or the most representative fragments (i.e. the signals with the minimum contributions from the fragmentation of other desorbing species).

9. TPD data acquisition was started by simultaneously turning on the sample heating via PID controller on the Heat Wave electronics and the QMS (using the intensity vs time or the so called “trend” mode). At the same time, the DataQ software was also started which records time vs temperature data coming from the analog to digital converter (ADC) connected to the thermocouple mounted on the single crystal sample. The thermocouple voltage measurement was also corrected with a cold junction compensator that is present in the Heat Wave Electronics. Heating ramp was set to 1 K/s between 90 K and 770 K. Once the maximum temperature was reached, heating was stopped. After the experiment, using a home-made “Data Matcher” software, “temperature vs. time” data obtained from the DataQ software was synchronized with

the “QMS intensity vs time” data acquired by the QMS; in order to obtain “Desorption Channel intensity vs Temperature” data, which essentially constitutes a so called TPD spectrum.

2.4.3. Data-Matcher

Data matcher is a home-made signal processing code that has been developed in our research group (by Abouzar Tasouji Azar, Bilkent University Chemistry Department Undergraduate Sophomore, 2013 and E. Ozensoy). This software has been used to couple “temperature vs. time” data and the “QMS intensity vs time” data in an attempt to improve the TPD signal quality. This code assigns a temperature value for every time-dependent reading of the QMS for a given desorption channel. Since both temperature readings and mass spectrometer readings are in the time domain, an extra signal processing is needed to synchronize data so that we can plot mass spectrometer data versus temperature by omitting the time variable. Furthermore, the signal processing routine also computes an average temperature value (using the heating ramp rate and the starting time of the heat ramp) for each small time interval (i.e. 1 s) during the heating ramp and matches it with the QMS intensity data. Then, it computes an average temperature value for every second. Later, the heating ramp (i.e. temperature vs time) data was linearized by a regression method (simply by connecting the middle/mean point of the interval where averaging was made with the middle/mean value of the next averaging interval). In other words, the temperature value for the middle of a second is considered to be the average temperature in that second. In this way, the frequent unrealistic local temperature drops and digitalization of the TPD data (which are artifacts of data processing not corresponding to actual/experimental temperature drop) are successfully avoided.

3. RESULTS and DISCUSSION

3.1 LEED Pattern of the Clean Au (111) Single Crystal Surface

The Au (111) sample was cleaned by sputtering the surface with Ar+ ions followed by heating the sample up to 750 K in vacuum. LEED experiments were performed on this Au(111) surface to check the surface cleanliness.

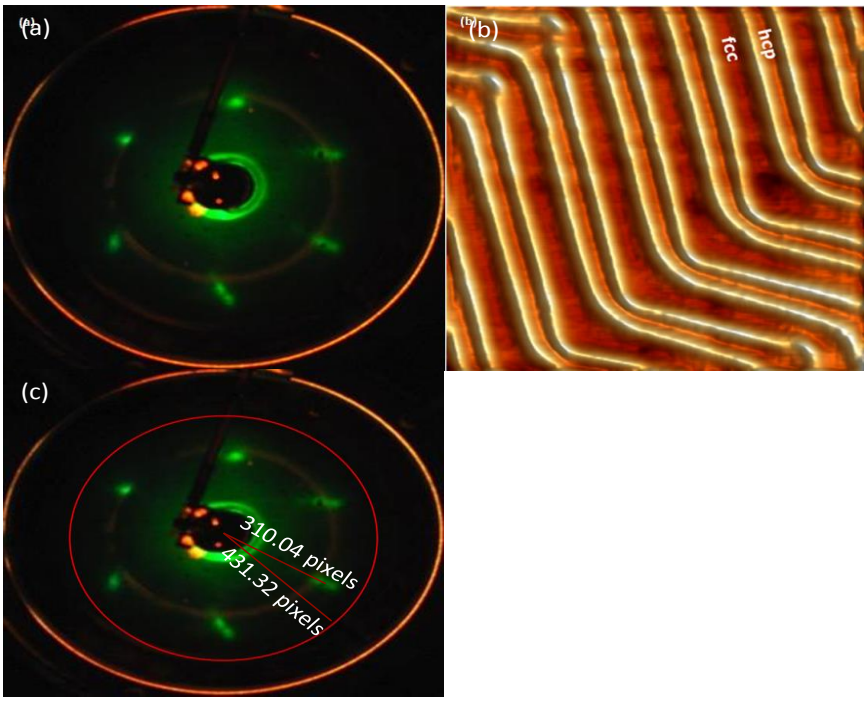

Figure 19. (a) LEED picture of the clean Au(111) surface recorded at 70 eV (current work). (b) Constant-current STM image of an area on Au(111) showing discommensuration lines of the 22×√3 surface reconstruction separating face-centered cubic fcc from hexagonal close-packed hcp stacking (ref 115). (c) LEED pattern with measured dimensions.

The actual distance between the gold atoms on the atomically clean Au(111) surface measured using the LEED image given in Figure 19(a) is presented in *Table 2*. The beam of electron has

been set to 70 eV of energy and the observed diffraction pattern is used to calculate the diameter of the screen in unit of pixed. Thus, radius of the experiment screen was calculated. We measured the opening angle and determined the distance between the gold atoms from the reciprocal image. Our calculations suggest that the Au-Au interatomic distance on the Au(111) surface is c.a. 2.88 A^{o} which has an excellent agreement with the previous data reported in the literature [121].

Table 2. Calculation of Au-Au interatomic distance on Au(111) using the LEED analysis

S.No	Energy (eV)	radius from LEED screen (pix.):	opening angle of the screen (º):	radius from the LEED point (pix.):	radius screen:	distance (Å)
1	70	431.32	45	310.04	610.7251909	2.88

The clean Au (111) surface produces a relatively sharp LEED pattern as shown in Figure 19(a). The observed pattern confirms the hexagonal symmetry of the Au(111) surface and the expected unit cell[114]. Some diffraction spots are observed fuzzy due to corrugations originating from (Fig 17(b)) the herringbone reconstruction of the Au(111) surface, which has been previously confirmed by STM experiments [115].

3.2 Hypothesis of the Current Work

TPD experiments were performed for different oxygenates to understand the nature of the interaction between the adsorbates and the Au(111) single crystal surface. The study of literature on partial oxidation reaction gave us an insight into the factors affecting the catalytic selectivity of au surfaces. These assessments led us to propose the following hypothesis to be investigated in the current work:

"Selectivity of Au(111) single crystal model catalyst surfaces in Partial Oxidation (PO) reactions are closely associated with the adsorption or desorption energy of the PO product that is generated through the reaction. In other words, a PO product with a low adsorption or

desorption energy will have a short residence time on the surface and thus can avoid total oxidation to CO_2. This leads to a higher catalytic selectivity towards that particular product"

In order to prove our hypothesis, we carried out adsorption experiments on the clean Au(111) single crystal model catalyst surface at liquid N_2 temperatures under UHV conditions using a variety of oxygenates and performed successive TPD measurements. Then, by applying the Redhead method on the TPD data, we have obtained experimental desorption energies for a variety of adsorbates. Finally, by comparing the relative desorption energies with the product formation likelihood of a particular molecule in a PO reaction, we have established the link between the catalytic selectivity and desorption energy.

3.3 TPD Analysis of Organic Molecule Adsorption on Au (111)

We performed alcohol, aldehyde, acetone, and ester adsorption on the clean Au(111) surface. These compounds have extremely small sticking coefficients on Au(111) at room temperature. Thus, the adsorption experiments were performed at 90 K after the Au(111) single crystal sample was cooled via liquid nitrogen. On the clean Au(111) surface, these oxygenates are weakly adsorbed and thus typically desorb molecularly in a reversible fashion. All of these compounds (purity >99.8%, Sigma-Aldrich) were additionally purified by subsequent freeze, pump and thaw cycles to remove contaminations such as N_2, H_2O and O_2.

Our Temperature Programmed desorption experiments are schematically described in Figure 20 given below. The Au(111) was exposed to a particular adsorbate. Then desorption of the adsorbate starts with the ramp in temperature. Generally, desorption occurs with two different features i.e multilayer (low temperature) and monolayer (high temperature) signals.

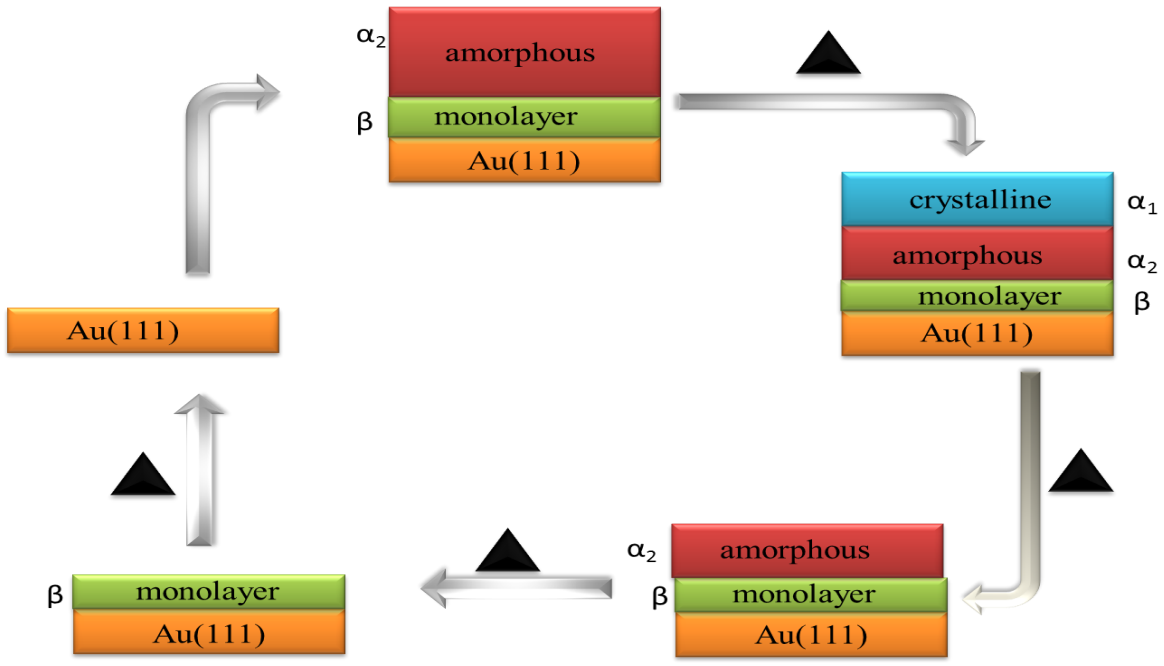

Figure 20 . TPD scheme representing the desorption of adsorbate from the Au(111) surface.

3.3.1 Adsorption and Desorption of Alcohols on Au(111)

Alcohol TPD spectra collected over Au(111) single crystal model catalyst surface are shown in Figures 22, 24, 27 and 29. The evolution of the alcohol is monitored using the m/z= 31 signal (corresponding to the methoxy or CH_3O- fragment), which is the most intense fragment in the mass spectrum of gas-phase alcohols. Alcohols were the only desorption product detected in TPD experiments after dosing alcohols on the clean Au(111) surface at 90 K.

a. Methanol

Methanol is the simplest of all alcohols. Generally it would be quite convenient to start with it, in order to understand the nature of alcohols. TPD spectra of methanol from clean Au(111) surface are shown in the Figure 22(a). A number of ion fragments (shown in the Figure 21) were measured, however no surface dissociation product were identified during the sample heating.

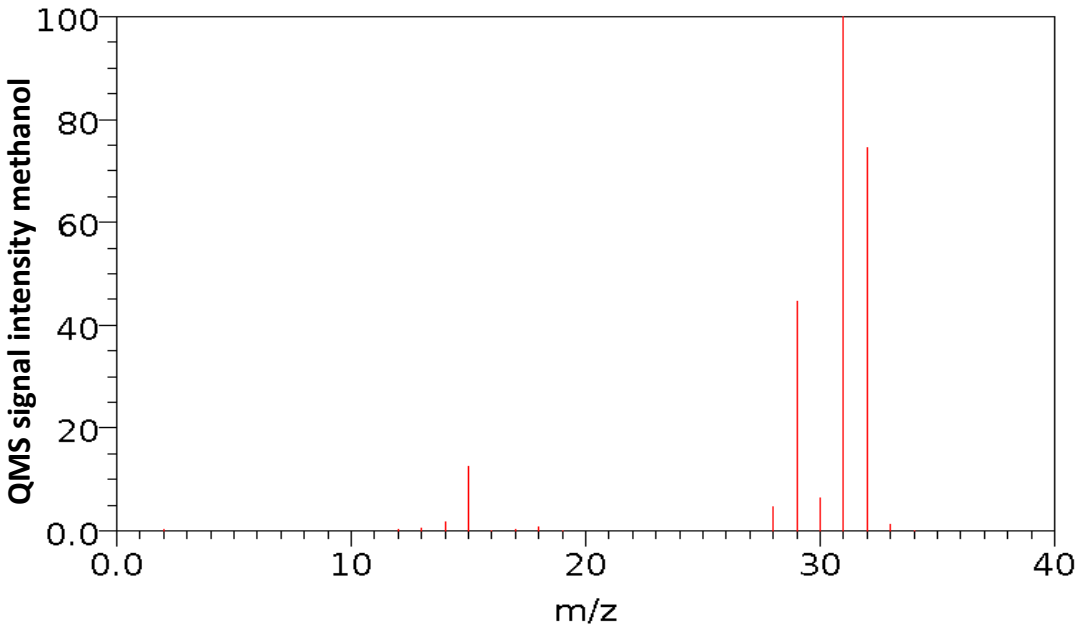

Figure 21. Mass fragmentation pattern of gaseous methanol (Permission requested for the reproduction from ref 122)

Repeated experiments without cleaning between successive measurements showed that, TPD spectra of methanol is highly reproducible. Thus, we conclude that methanol adsorbs and desorbs molecularly on Au(111) surface. Desorption signal for the most intense fragment of methanol (i.e. mass to charge *(m/z)* ratio of 31) are shown in the Figure 22 for different adsorbate coverages ranging from 0.07 L to 6.9 L (1 L= 10^{-6} Torr.s). The TPD spectra show three distinct peaks which we denote as α_1 , α_2 and β. The β peak fills at the lowest coverage and desorbs at a higher temperature of 155 K and therefore is assigned to methanol monolayer, adsorbed on the Au(111) surface which ultimately desorbs in 1^{st} order fashion. Peaks α_1 and α_2, the multilayer features, appear as the methanol exposure increases. Zero order desorption takes place in the multilayers. This multilayer can be attributed to crystalline (α_1) and amorphous (α_2) structures, respectively. However, there is one peak at high temperature as shown in the *inset*, which has not been reported in the literature. We suggest that this feature comes from the desorption of methanol from the defects caused by sputtering the surface or it may be due to recombinative desorption. It is likely that we have point and extended defects on the surface (including the ones originating from herringbone reconstruction) where

methanol adsorbs more strongly. Our experimental results for methanol coincides with the TPD results from the literature as shown in Figures 22 (a) and (b).

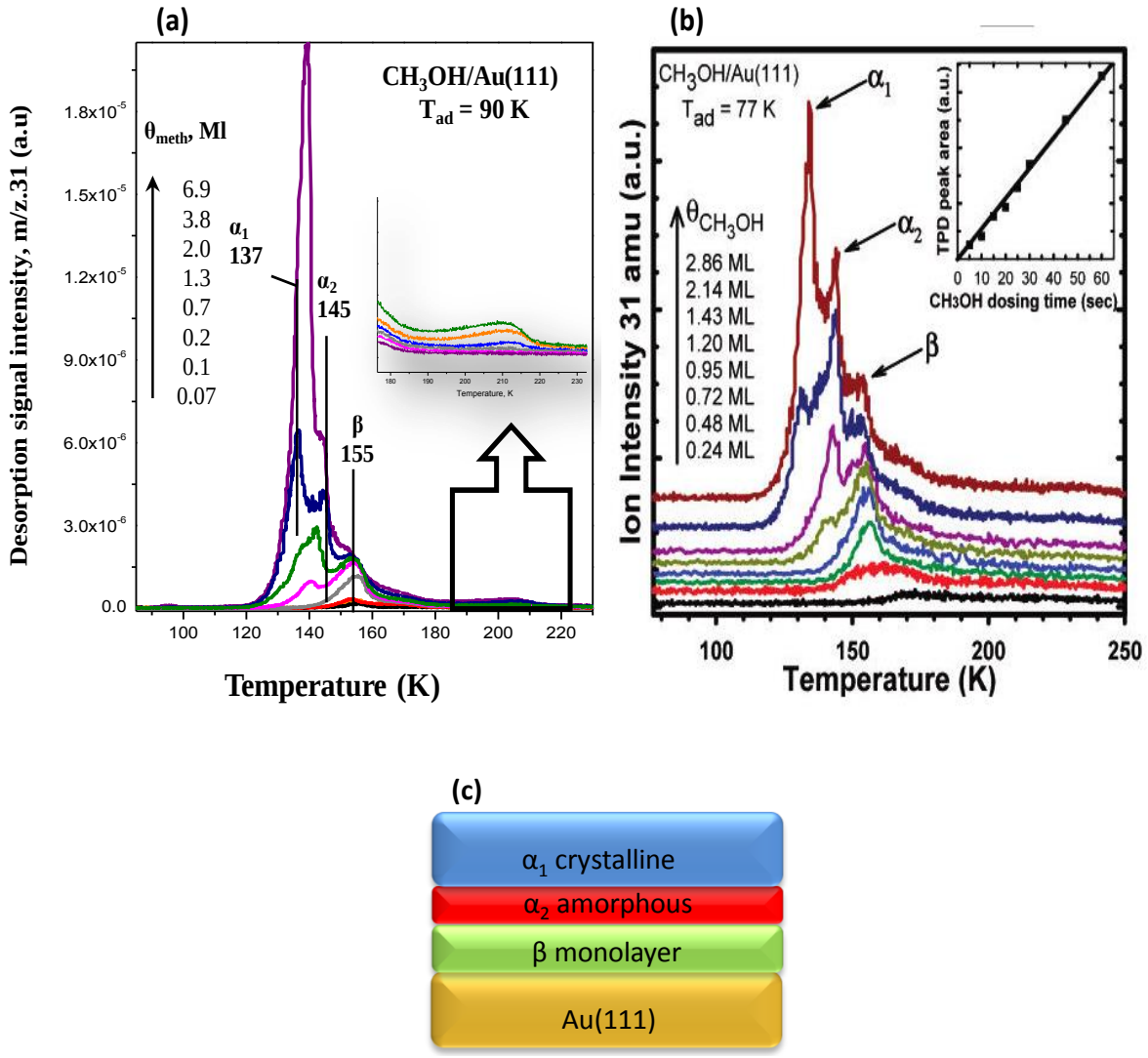

Figure 22. (a) TPD spectra corresponding to various coverages of methanol (a) current work, (b) Ref 116. (Permission requested for the reproduction from ref 116). Schematic representation of desorption behavior.

b. Ethanol

TPD experiments have also been performed with ethanol adsorbed on clean Au(111) surface. As in the case of methanol, ethanol desorption is also monitored by m/z=31 desorption signal, which is the most intense in the gas-phase ethanol mass spectrum as well (Figure 23). In contrast to methanol TPD, ethanol desorption curves also have some contribution from H_2O desorption (m/z = 18) which reveals itself as a sharp ethanol desorption peak at 150 K (shown in Figure 24). This water signal is related to the humidity (i.e. contamination) in dosed ethanol flux. Our data coincide with the previously reported data for ethanol desorption, with only one exception i.e with the addition of water peak at 153 K. This is not surprising as it is well known that ethanol is difficult to purify from water. In the current experiments, we utilized ethanol with 99.8% purity and purified it additionally with freeze-pump-thaw cycles. However even after such a careful purification protocol, presence of a minor amount of water can be detected via the high sensitivity of the TPD technique.

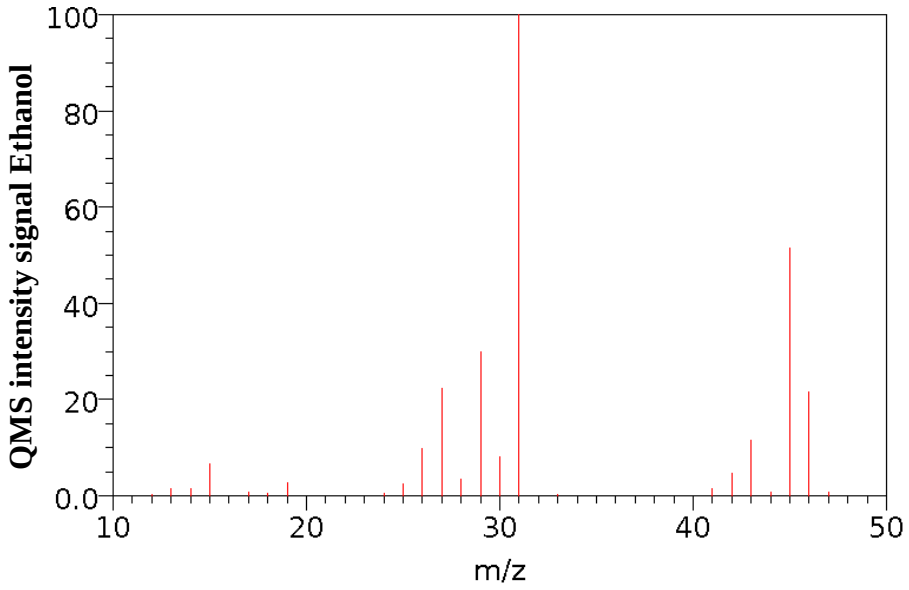

Figure 23. Mass fragmentation pattern of gaseous ethanol.(Permission requested for the reproduction from ref 122)

At low ethanol exposures the TPD spectra show a single symmetric peak at 196 K, which we tentatively label as β referring to ethanol monolayer. The saturation of this peak was used for estimating the ethanol coverage and like in the case of methanol was presumed to be 1 ML. When the ethanol surface coverage exceeds 1 ML, the α peak at 175 K appears which is

associated with multilayers adsorbed on the top of monolayer (β) ethanol. With the increase of the coverage this peak monotonically rises, finally overlapping and covering the β peak. At very high exposures, a new sharp peak at 153 K can be observed. This peak was tentatively associated with the desorption of $C_2H_5OH \cdot xH_2O$ phase; this assignment is in the agreement with the water desorption at the same temperature as shown in the Figure 25.

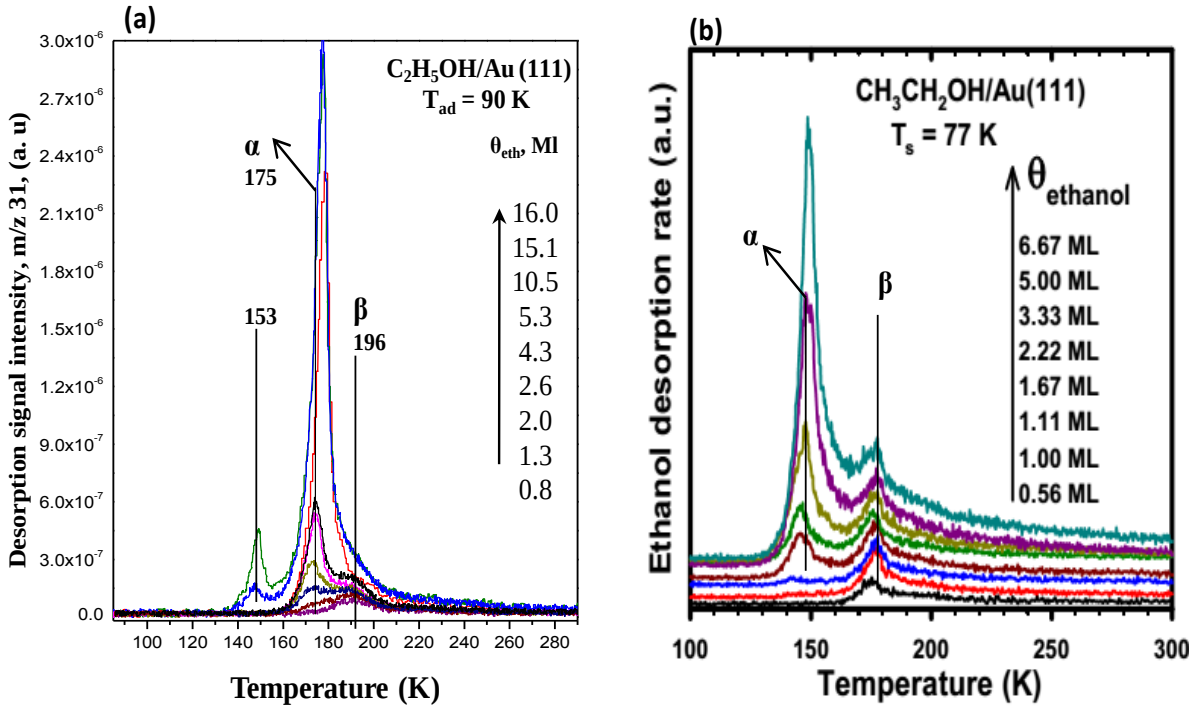

Figure 24. (a) TPD spectra corresponding to various coverages of ethanol on clean Au(111) (a) current work, (b) from Ref 117. (Permission requested for the reproduction of ref 117). (c) schematic representation of desorption behavior.

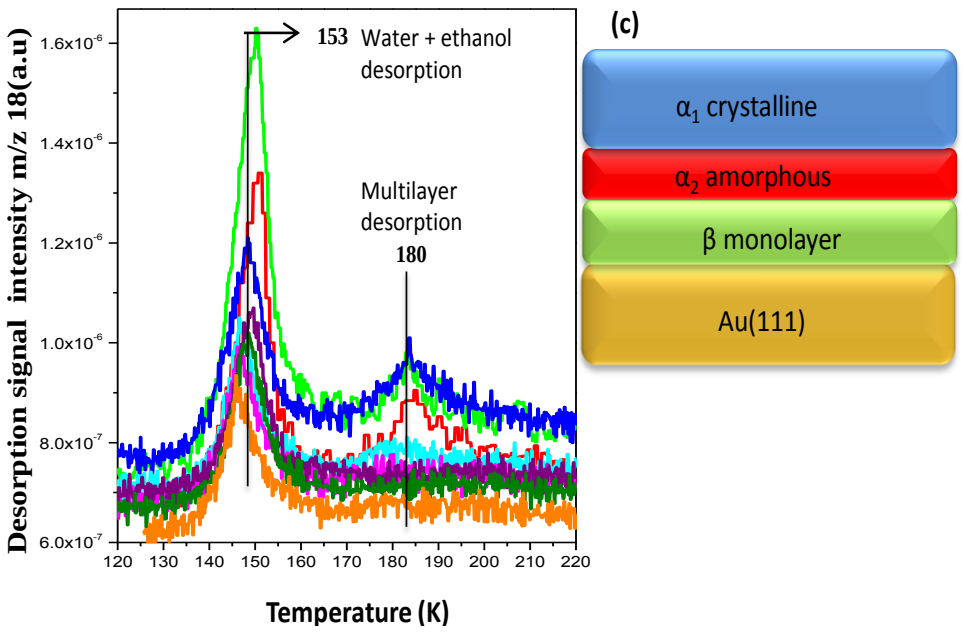

Figure 25. (a) m/z= 18 TPD spectra corresponding to various coverages of ethanol on clean Au(111) (current work).

Gong et al. studied ethanol desorption on A(111) as shown in the Figure 24(b). Multilayer consisted of two peaks where α_2 was attributed to the amorphous phase and α_1 to the crystalline phase. In other words, crystalline phase forms from amorphous phase during the heating process but not all amorphous phase turns into crystalline.

C. Propanol

1-propanol (≥99% purity, Sigma-Aldrich) was adsorbed on clean Au(111) single crystal surface at 90 K. The 1-propanol gas phase mass spectrum is shown in Fig 26. 1-propanol evolution is monitored using the m/z 31 signal, corresponding to the most intense fragment in the mass spectrum of gas-phase 1-propanol *(Figure 27)*. The other fragments of the mass spectra also demonstrate exactly the same TPD line shape with the m/z = 31 signal.

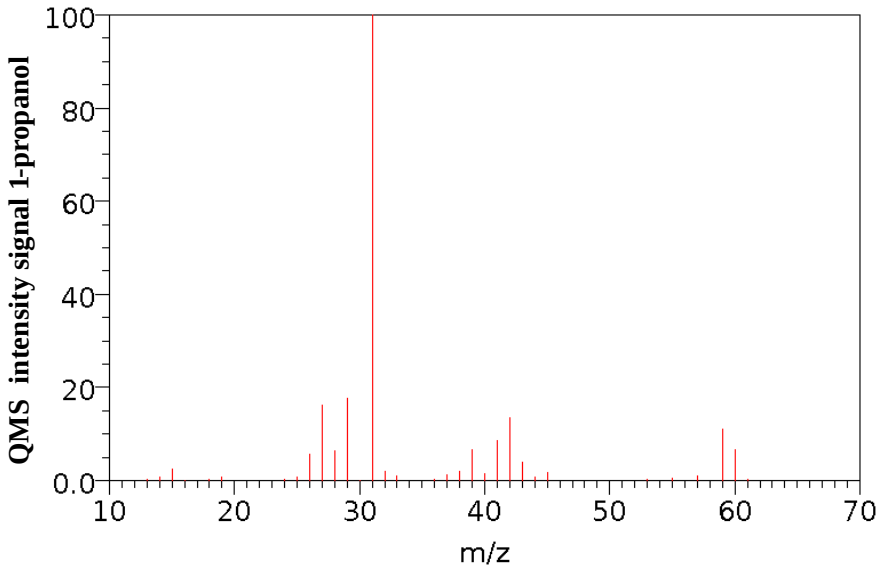

Figure 26. Mass fragmentation pattern of gaseous 1-propanol. (Permission requested for the reproduction from ref 122)

TPD data for 1-propanol from Au(111) surface suggests a non-dissociative adsorption behavior as no additional desorption signals were detected other than the expected signals of the nascent adsorbate *(Figure 27(a))*. The monolayer desorption peak grows with exposure and saturates at 202 K. The multilayer desorbs as two overlapping peaks at 168 and 174 K. These two multilayer peaks are tentatively assigned to crystalline and amorphous layers, respectively.

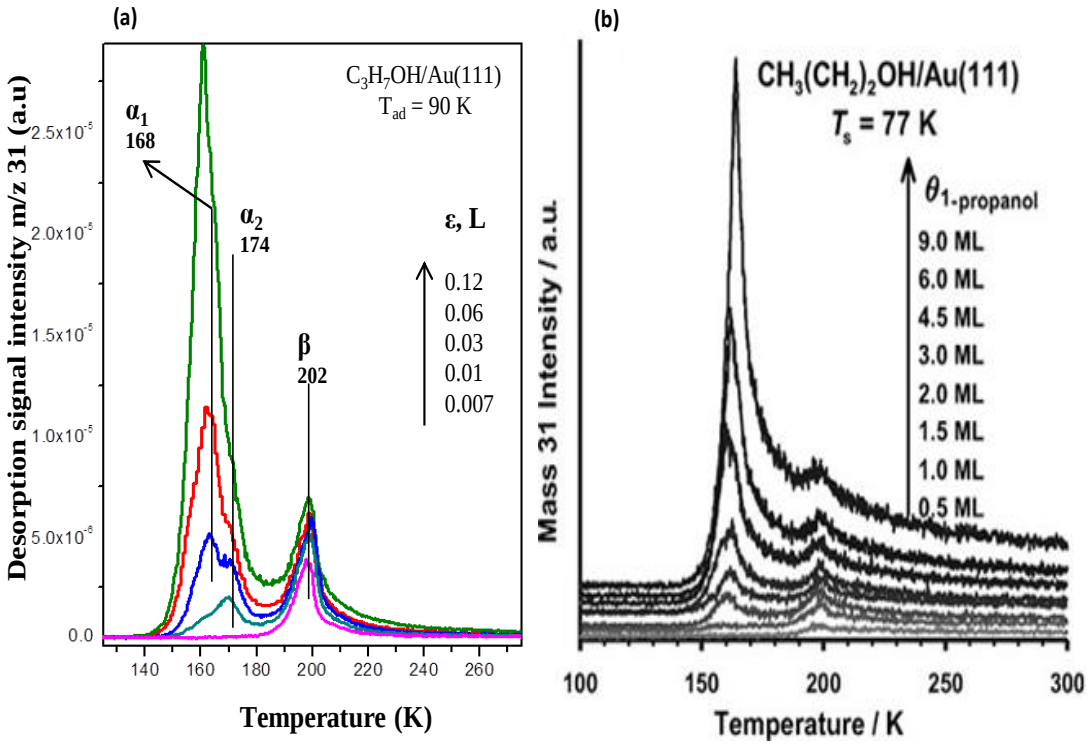

Figure 27. TPD spectra corresponding to m/z = 31 for various exposures of 1-propanol on clean Au(111) (a) current work and (b) from Ref 118 (Permission requested for the reproduction from ref. 118).

2-propanol (≥99.5% purity, Sigma-Aldrich) was exposed to clean gold single crystal surface at 90 K. Fragmentation of the 2-propanol in a regular Residual Gas Analysis (RGA) experiment is given in Figure 28 [122].

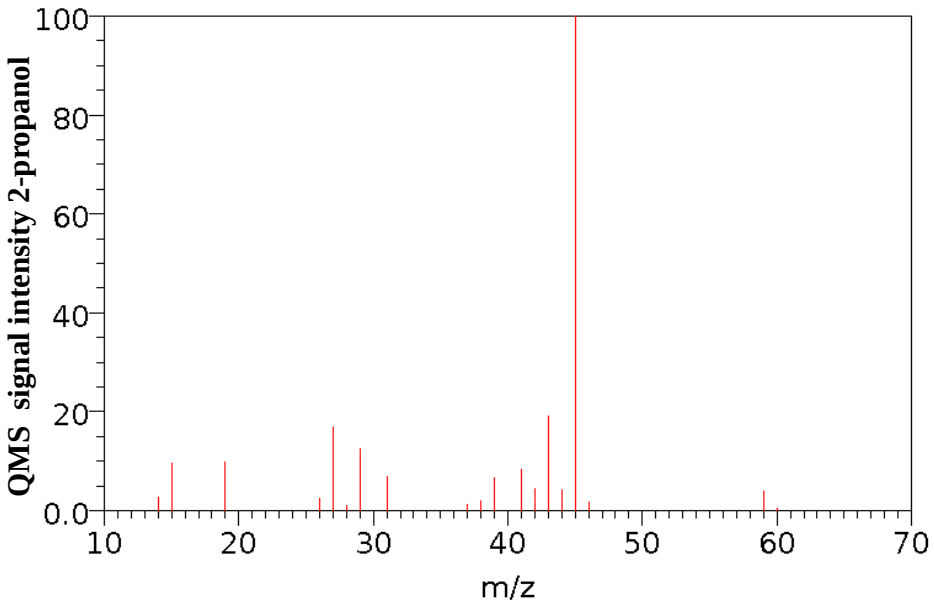

Figure 28. Mass fragmentation pattern of 2- propanol. (Permission requested for the reproduction from ref 122)

2-propanol desorbs from Au(111) surface non-dissociatively as described earlier. The monolayer desorption peak is observed at 187 K. The multilayer desorbs as two peaks at 154 and 164 K; by analogy these peaks are associated with crystalline and amorphous layers, respectively.

Gong et al. [118] carried out similar investigations of 2-propanol on Au(111) as shown in *figure 29 (b)*. The desorption behavior and the temperature profiles are similar to TPD data shown in *figure 29(a)*. Our data is much more clear, as the desorption features are much better resolved from each other than the one reported in the literature.

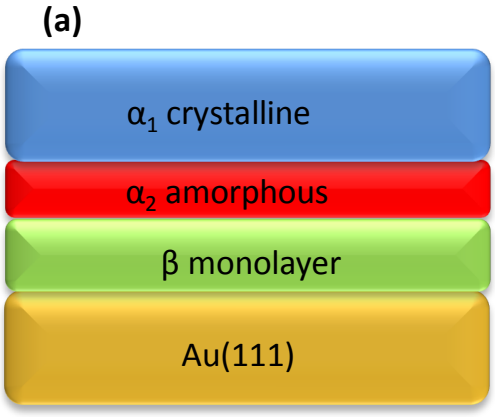

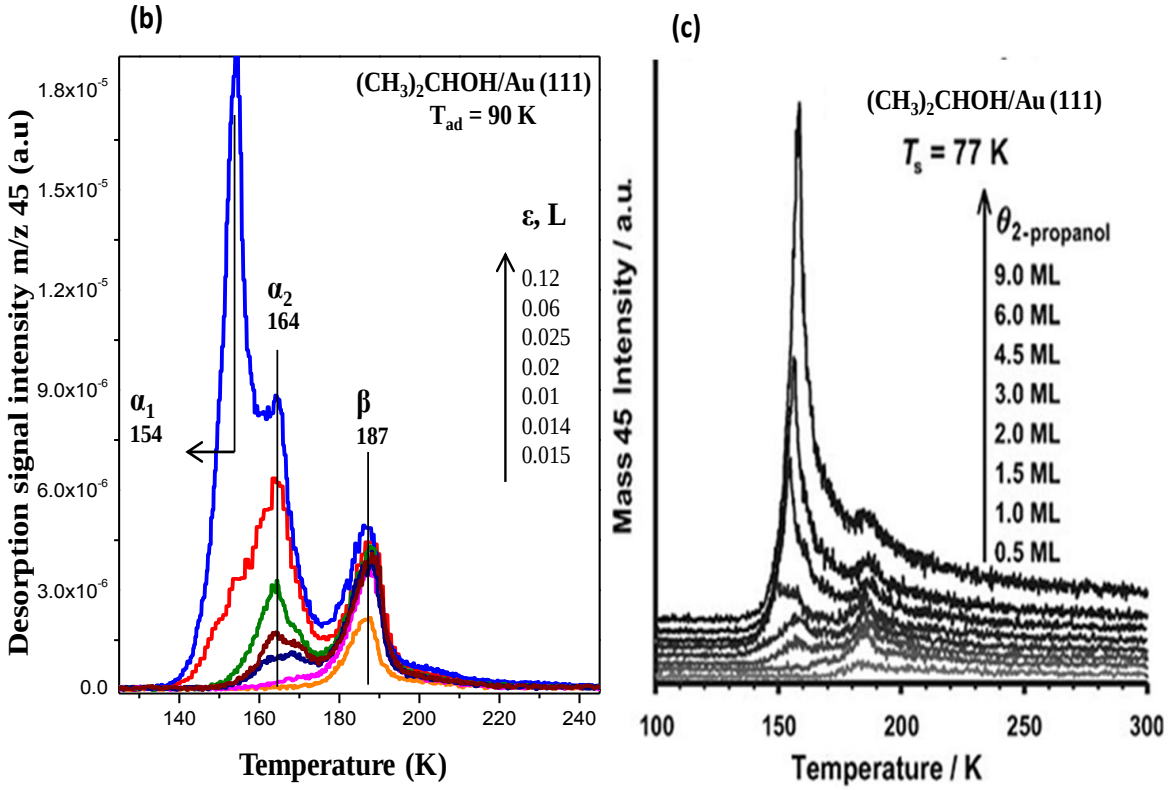

Figure 29 . TPD spectra corresponding to various exposures of 2-propanol on clean Au(111) (b) current work and (c) from Ref 118. (Permission requested for the reproduction from ref. 118)

3.3.2 Ethers

The diethyl ether desorption behavior is studied by monitoring the most intense fragment having a m/z ratio of 31 *(Figure 30)*.The TPD spectra of various coverages of diethyl ether on Au(111) surface are presented in *Figure 31(a)*. The various desorption channels corresponding to some of the mass fragmentation products were also measured but diethyl ether dissociation was not detected on the Au(111) surface.

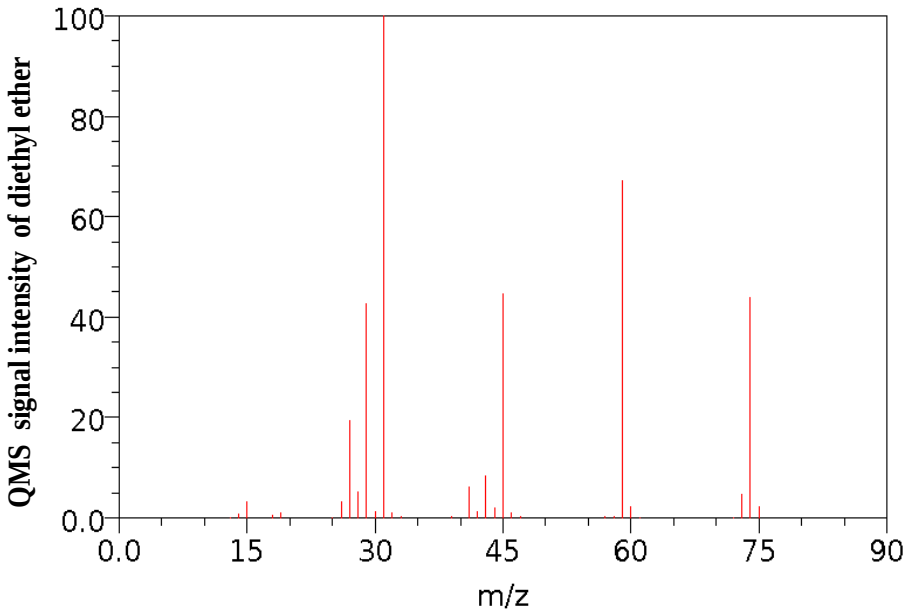

Figure 30. Mass fragmentation pattern of gaseous diethyl ether. (Permission requested for the reproduction from ref 122)

Multilayer desorption occurs in a zero order fashion at c.a. 124 K. The peak at 182 K which is saturating with increasing exposure with a first order behavior can be attributed to the desorption of diethyl ether monolayer on the Au(111) surface. The peak at 144 K can be assigned to the second adsorbate layer demonstrating a higher thermal stability than the other multilayers. Interestingly this intermediate layer can be saturated and the total quantity of molecules in this layer is less than the first monolayer (approximately by a factor of 1/2). Thus, the second layer can be associated to a layer revealing a lower 2D density *Figure 31(c)* than the first monolayer. The dissimilarity in the packaging structures of the first and the second layers can be correlated to differences in the interaction of the first diethyl ether layer with the Au (111) surface and the interaction between the second diethyl ether layer located on the top of the first diethyl ether monolayer.

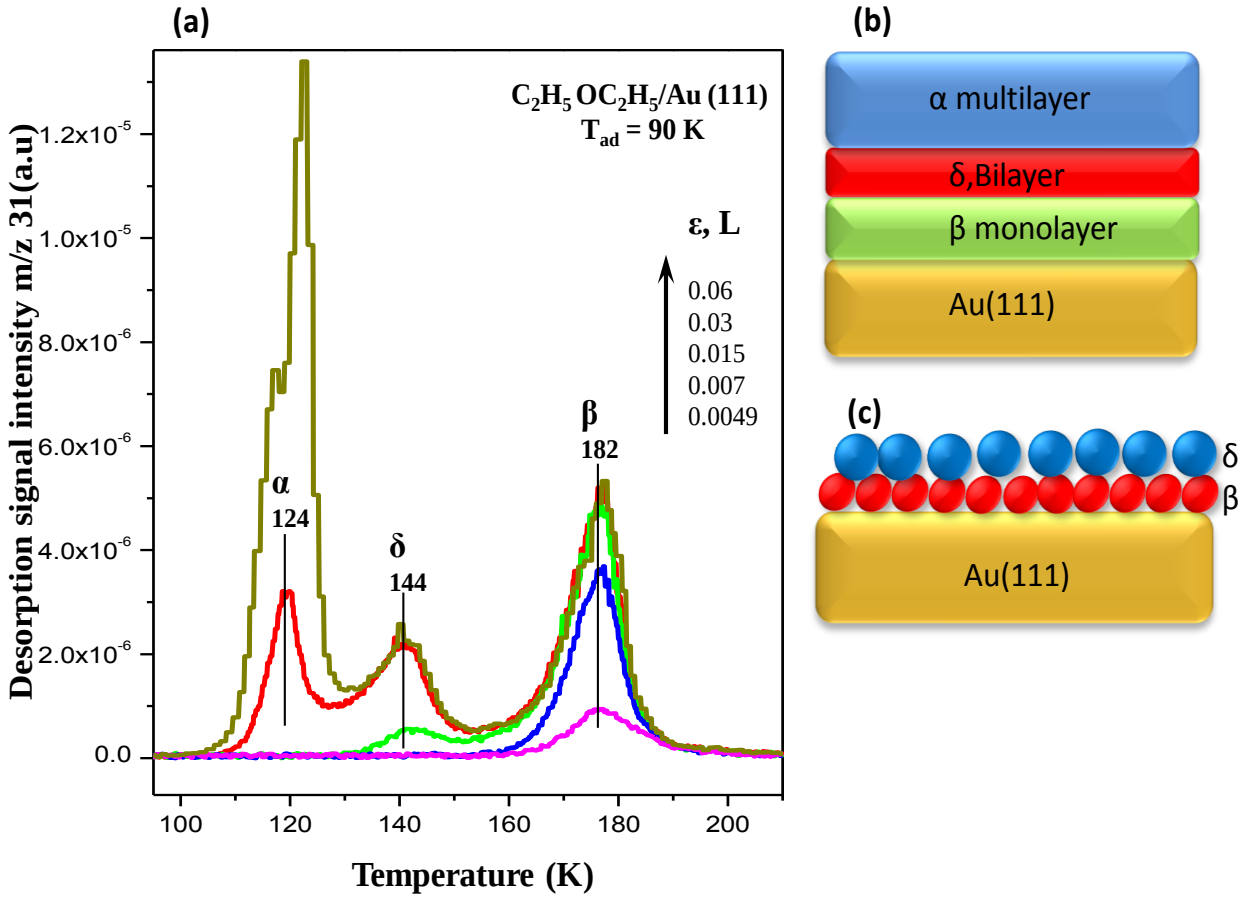

Figure 31 (a)TPD spectra corresponding to various exposures of diethyl ether dosed onto clean Au(111) at 90 K. Schematic presentation of DEE adsorption: (b) general adsorption features, (c) difference in the packing density of β and δ structures where β has a %50 lower packing density.

3.3.3 Aldehydes

a. Acetaldehyde

Acetaldehyde desorbs from the metal surfaces in a very complicated fashion, as reported, revealing two molecular adsorbate configurations [η^1(O) and η^2(C,O)] as well as polymeric forms of acetaldeyhe monomer (i.e. pol-yacetaldehyde)[106,107]. Acetaldehyde RGA spectrum

is given in *Figure 32* while TPD spectra are presented in *Figure 33(a)*. The peaks at 118 and 125 K which are observed at high acetaldehyde exposures correspond to the multilayer desorption signals, desorbing with a zero order desorption kinetics. The peak at 138 K appearing and quickly saturating at the initial stages of adsorption is associated with the monolayer desorption (revealing 1st order desorption behavior). In previous studies it was concluded that acetaldehyde is able to polymerize on the gold surface [105]. In our experiments with increasing exposure, we have detected new high temperature desorption signals at T > 195 K. With the appearance of the 195 K desorption peak, the already saturated monolayer peak at 135 K is altered (i.e. intensity of the latter feature decreases and its maximum shifts to 132 K).

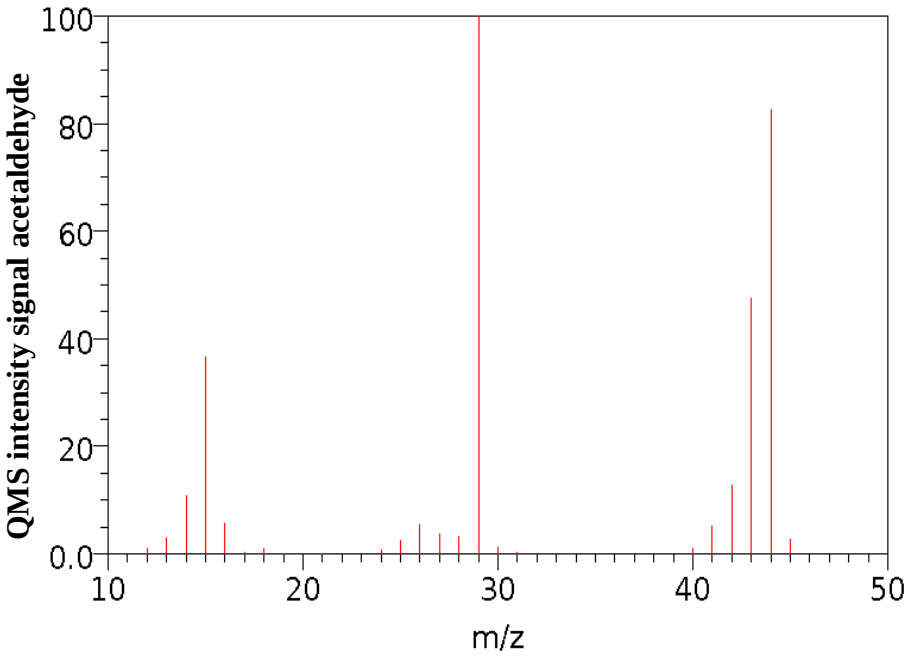

Figure 32. Mass fragmentation pattern of acetaldehyde. (Permission requested for the reproduction from ref 122)

These changes in the monolayer related peak can be associated with the formation of 2D polymer agglomerates which occupy some of the Au(111) surface sites, decreasing/replacing some of the monomeric acetaldehyde molecules in the first layer. Further increase of exposure leads to the evolution of multilayer peaks and the appearance of another high-temperature

feature at 202 K. This 202 K peak, can also be attributed to the decomposition of thermally stable 2D polymeric agglomerates.

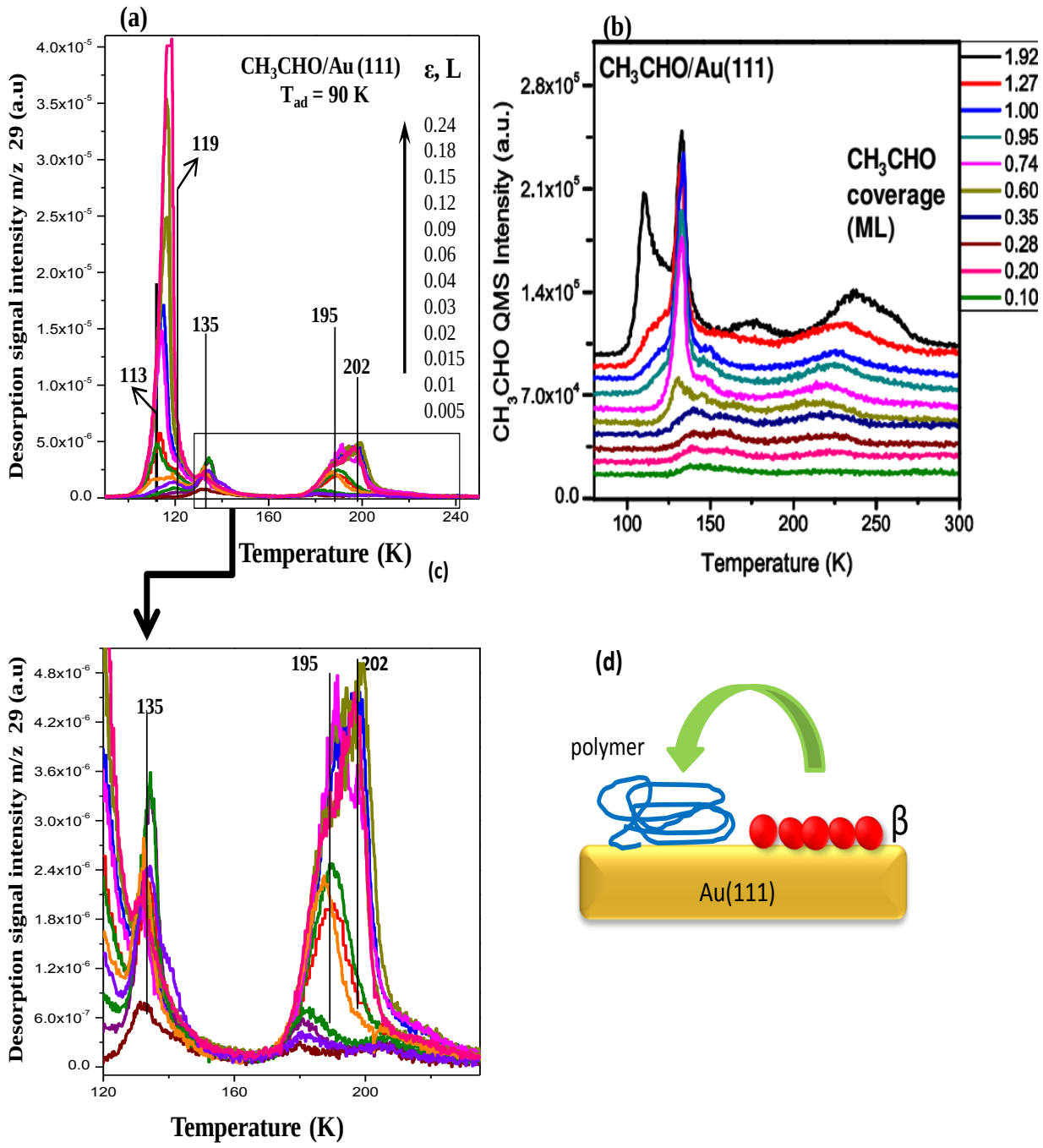

Figure 33. TPD spectra corresponding to various exposures of acetaldehyde dosed onto clean Au(111) at 90 K, (a) current work, (b) from Ref [105] c) detailed presentation of the high

temperature desorption window indicating the polymerization of acetaldehyde on Au(111) (current work). (d) showing conversion of monolayer into polymer.

A closer look at the spectrum shown in *Figure 33(c)* reveals that high temperature desorption features appear at higher exposures. We postulate that this feature is due to the decomposition of two dimensional polymerized acetaldehyde on the surface, bonded through η^2(C,O) CH_3CHO configuration. In our data shown in the *Figure 33(a)* the desorption features are well separated compared to the previously reported data in the literature *(shown in Figure 33(b))*. A more detailed analysis of the *Figure 33(c)* suggests that there are different types of polymer formation. The suggested resonance structure of acetaldehyde is shown in the *Figure 34*. The resonating structure stabilizes the acetaldehyde on the surface and thus ultimately results into polymerization.

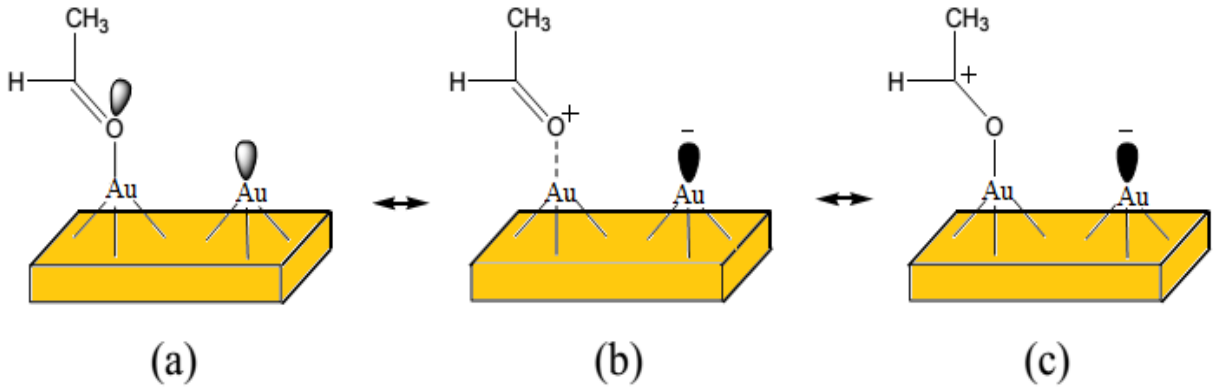

Figure 34. Resonance [(b) and (c)] and charge-transfer (a) structures of η^1(O) acetaldehyde on Au(111) surface (Adapted from ref 120).

b. Polymerization mechanism:

The suggested mechanism for the polymerization of acetaldehyde is shown in *Figure 35*. Acetaldehyde adsorbs on the surface through its oxygen (i.e. η^1(O) CH_3CHO configuration) *(Figure 36)*.

This creates a carbocation, and is thus susceptible to be attacked by another acetaldehyde monomer. In this way, acetaldehyde monomers polymerize to form various polymers *(Figure 36)*.

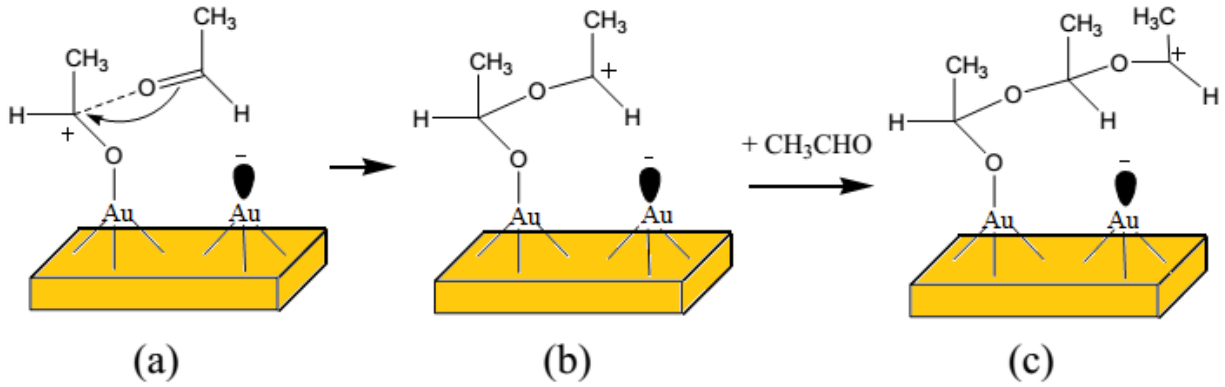

Figure 35. Polymerization pathway of acetaldehyde on Au(111) (Adapted from ref 120).

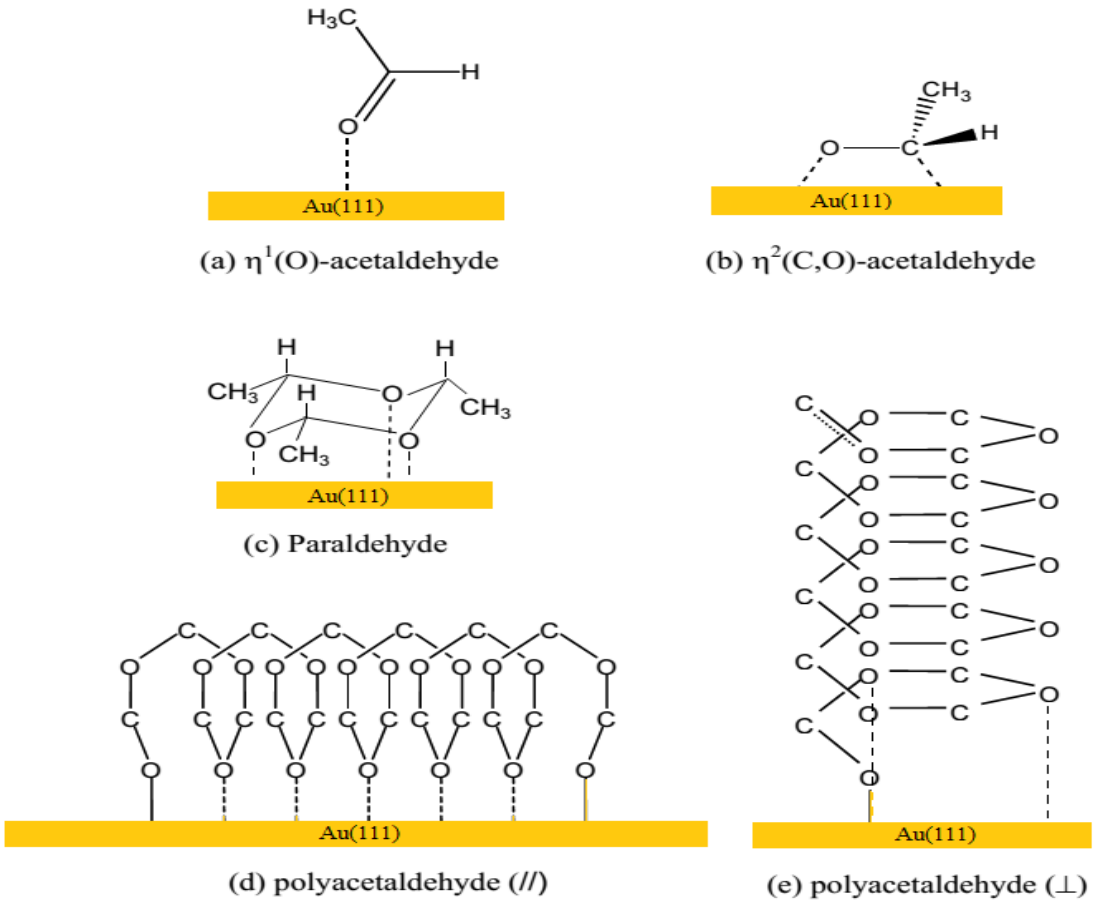

Figure 36. Possible adsorption configurations of monomeric, oligomeric and polymeric forms of

acetaldehyde on Au(111) (for polyacetaldehyde in d and e, CH_3 and H groups have been omitted for clarity) [Adapted from 119].

3.2.4 Ketones

Acetone (≥99% purity, Sigma-Aldrich) mass fragmentation is presented in *Figure 37*. TPD spectra of acetone from Au(111) after dosing at 90 K are presented in Figure 38. Desorption signals for various mass fragments of acetone were checked for any indications of acetone dissociation but acetone was found to desorb from Au(111) surface exclusively in a non-dissociative fashion. The most intense fragment (i.e. m/z = 43) was utilized to understand the desorption behavior as shown in the *Figure 38*.

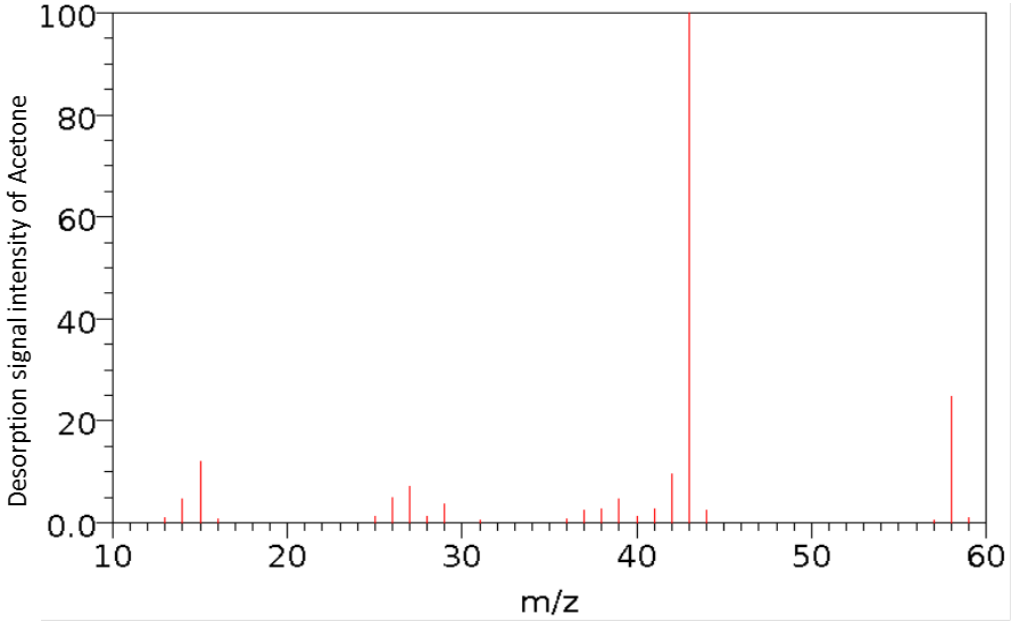

Figure 37. Mass Fragmentation pattern of acetone. (Permission requested for the reproduction from ref 122)

The TPD spectra of acetone are close to that observed for 1-propanol and 2-propanol. The monolayer desorption peak is observed at 159 K. The crystalline and amorphous multilayer peaks desorb in a zero order way and are observed at 136 and 141 K *(Figure 38)*. For acetone, one can note that amorphous layer (which is formed between crystalline layer and monolayer) demonstrates saturating behavior like monolayer. Furthermore, intensity of this peak is close to the monolayer one. Apparently the amorphous layer exists as only second layer over the first monolayer of acetone/Au(111).

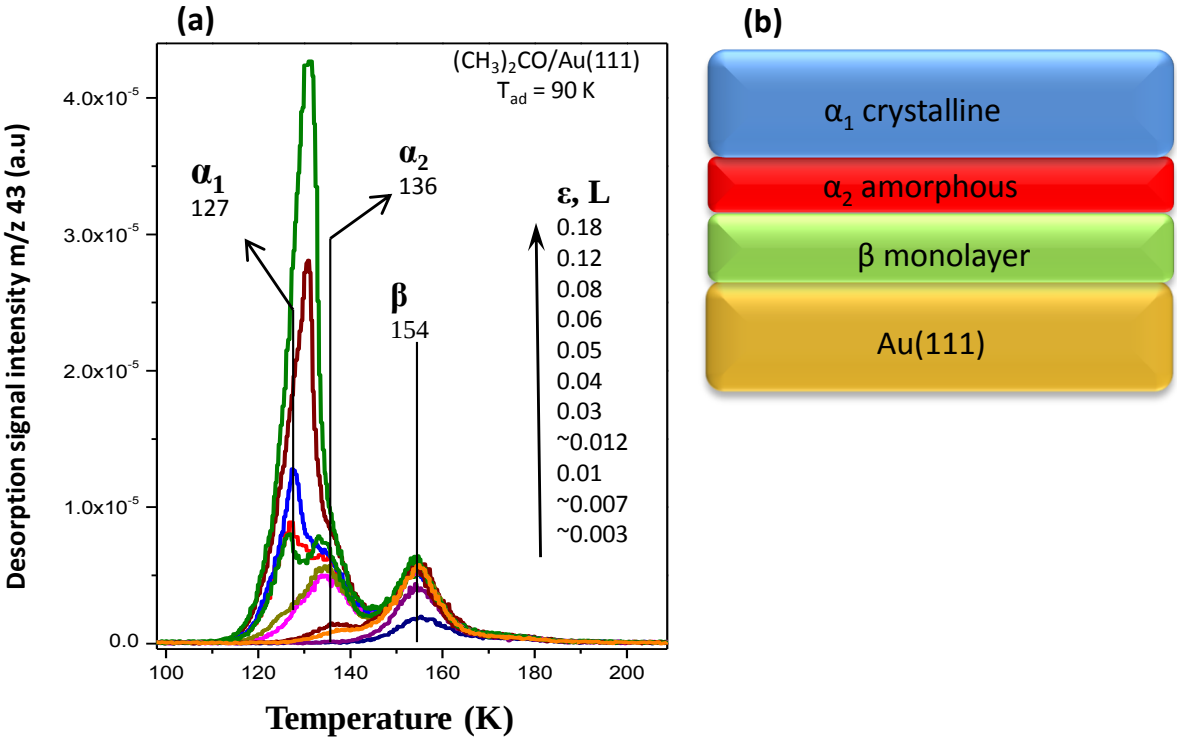

Figure 38. (a)TPD spectra corresponding to various exposures of acetone on clean Au(111) at 90 K. (b) Shematc representation of desorption behavior.

3.3.5 Esters

Methylformate and ethylformate mass fragmentation patterns are presented in *Figure 39*. TPD spectra obtained after methylformate dosing at 90 K are presented in *Figure 40(a)*. No methyl formate dissociation was observed on Au(111) surface after checking desorption signals of various mass fragments of methyl formate. The TPD spectra in *Figure 40(a)* are close to that presented for other chemicals; though monolayer and multilayer peaks are separated much better revealing distinct features. The saturating monolayer peak is pinned at 147 K. The overlapping multilayer peaks of crystalline and amorphous layers at 125 and 129 K shift to higher temperatures with increasing coverages *(Figure 40(a))*. These shifts are in agreement with zero order multilayer desorption behavior.

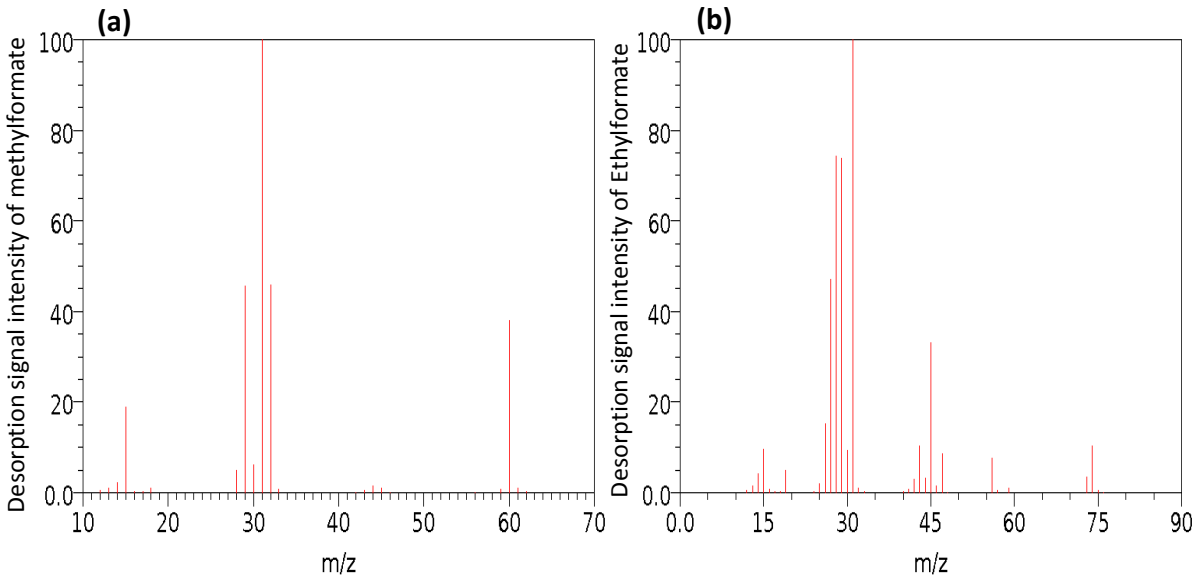

Figure 39. Mass fragmentation patterns of (a) methylformate and (b) ethylformate respectively. (Permission requested for the reproduction from ref 122)

Ethyl formate TPD spectra are presented in *Figure 40(b)*. Ethyl formate desorption was monitored utilizing the m/z = 29 desorption signal which is the most intense fragment. *(Figure 39(b))* No ethyl formate dissociation was observed on the Au(111) surface (i.e. the TPD line shapes of all other fragments are identical). The low temperature peaks at 138 and 151 K are associated with desorption of crystalline and amorphous multilayers, respectively. The small peak at 125 K can be associated with desorption of a small portion of amorphous, not crystallized yet ethyl formate. Here it should be noted that after the initial adsorbate dose at 90 K (i.e. at the beginning of the TPD experiments) the multilayer adsorbate overlayers are in amorphous form. The crystallization occurs during the heating at the initial stages of the TPD experiment. The behavior of high temperature desorption features of ethyl formate is more complicated than the other cases discussed above. At low exposures the monolayer related peak can be observed at 171 K *(Figure 40(b))*.

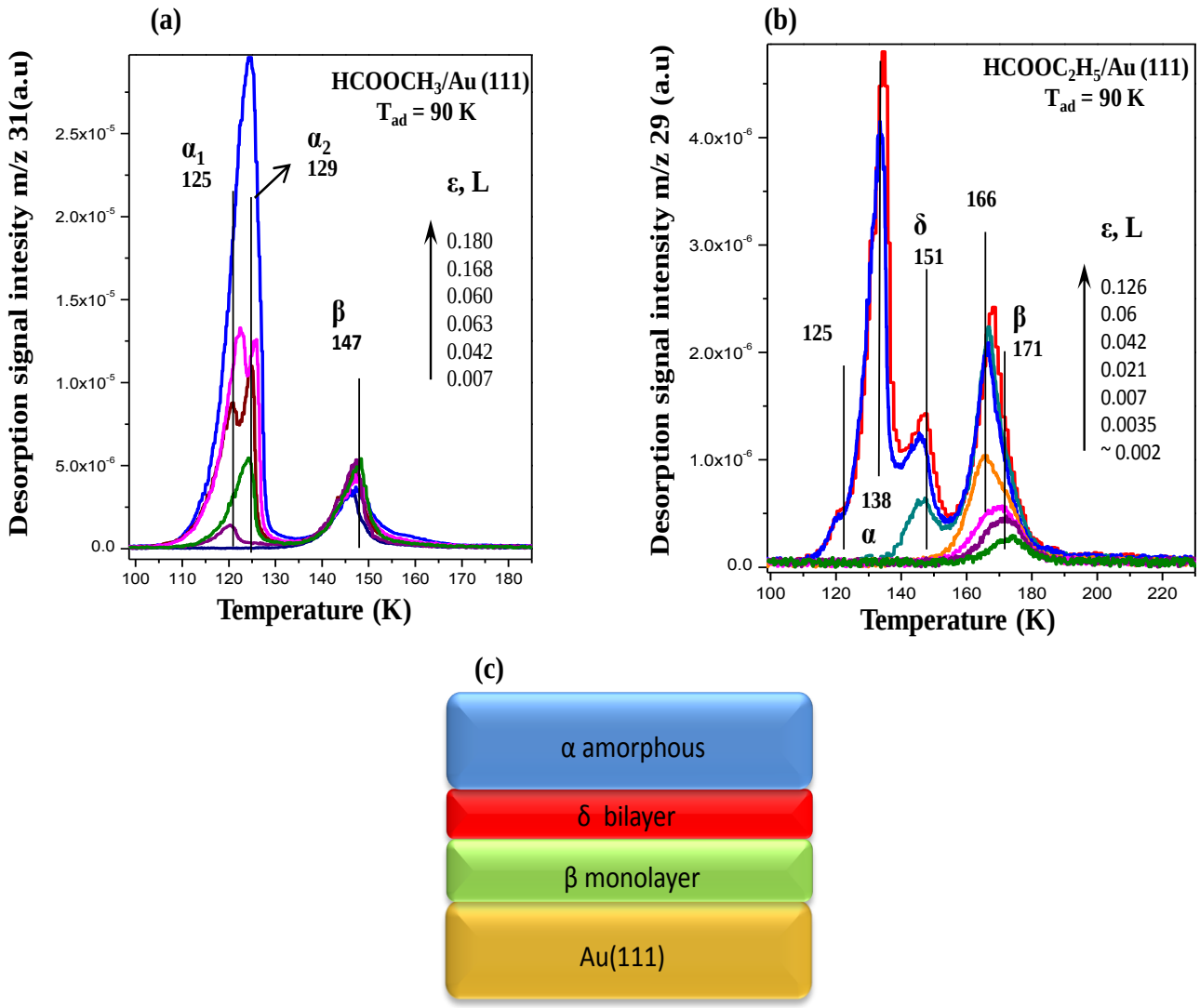

Figure 40. TPD spectra for corresponding to various exposures of (a) methyl and (b)ethyl formate dosed at 90 K onto clean Au(111). (c) schematic presentation of desorption.

Mass fragmentation of methylacetate and ethylacetate are given in Figure 41. Methyl acetate TPD spectra are presented in *Figure 42 (a)*. Methyl acetate was monitored utilizing the m/z = 43 desorption channel. No dissociation of methyl acetate was observed. One can observe overlapping and shifting of two peaks at c.a. 139 K which are associated with multilayer

desorption (probably crystalline and amorphous multilayers) and are zero order in nature. The monolayer desorbs from the surface at 172 K and corresponds to 1st order kinetics.

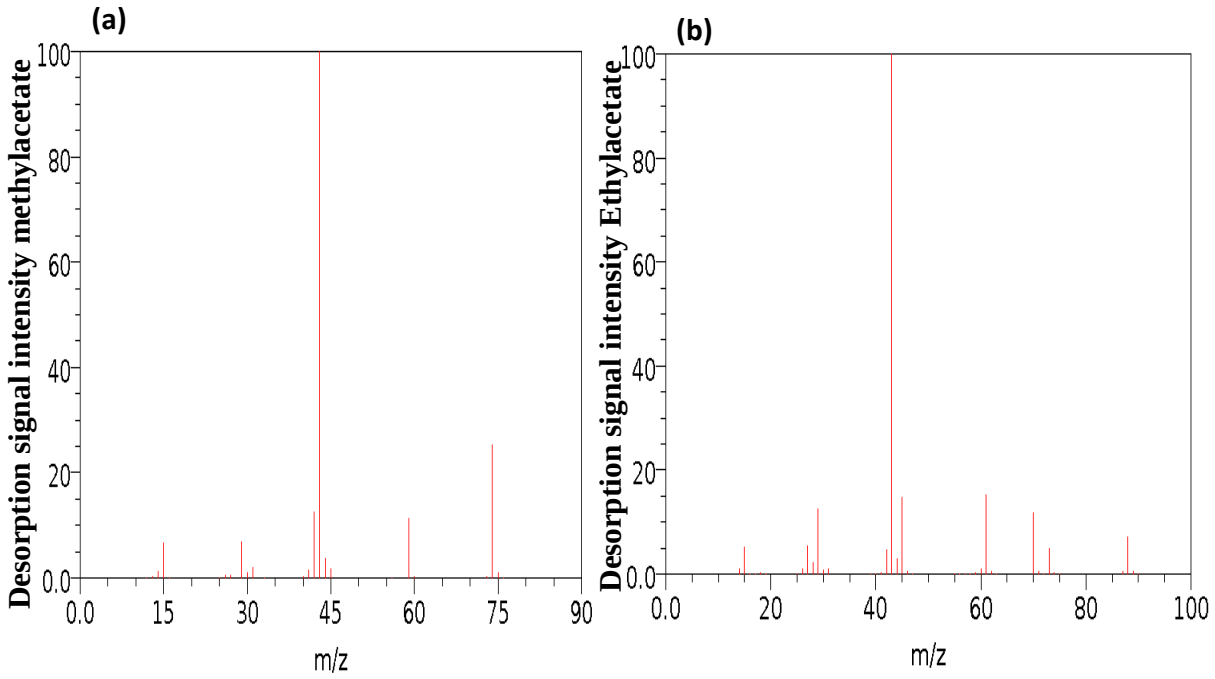

Figure 41. Mass fragmentation patterns of (a) methyl and (b) ethyl acetate. (Permission requested for the reproduction from ref 122)

Ethyl acetate TPD spectra are presented in *Figure 42 (b)*. For ethyl acetate monitoring we utilized the m/z = 43 channel *(Figure 41(b))*. Dissociation of ethyl acetate was not observed. The TPD spectra of ethyl acetate demonstrate only two peaks: peak at 150 K which are associated with multilayers (probably in crystalline form) revealing zero order desorption kinetics and the higher desorption signal located at 194 K, showing a first order desorption behavior corresponding to monolayer states.

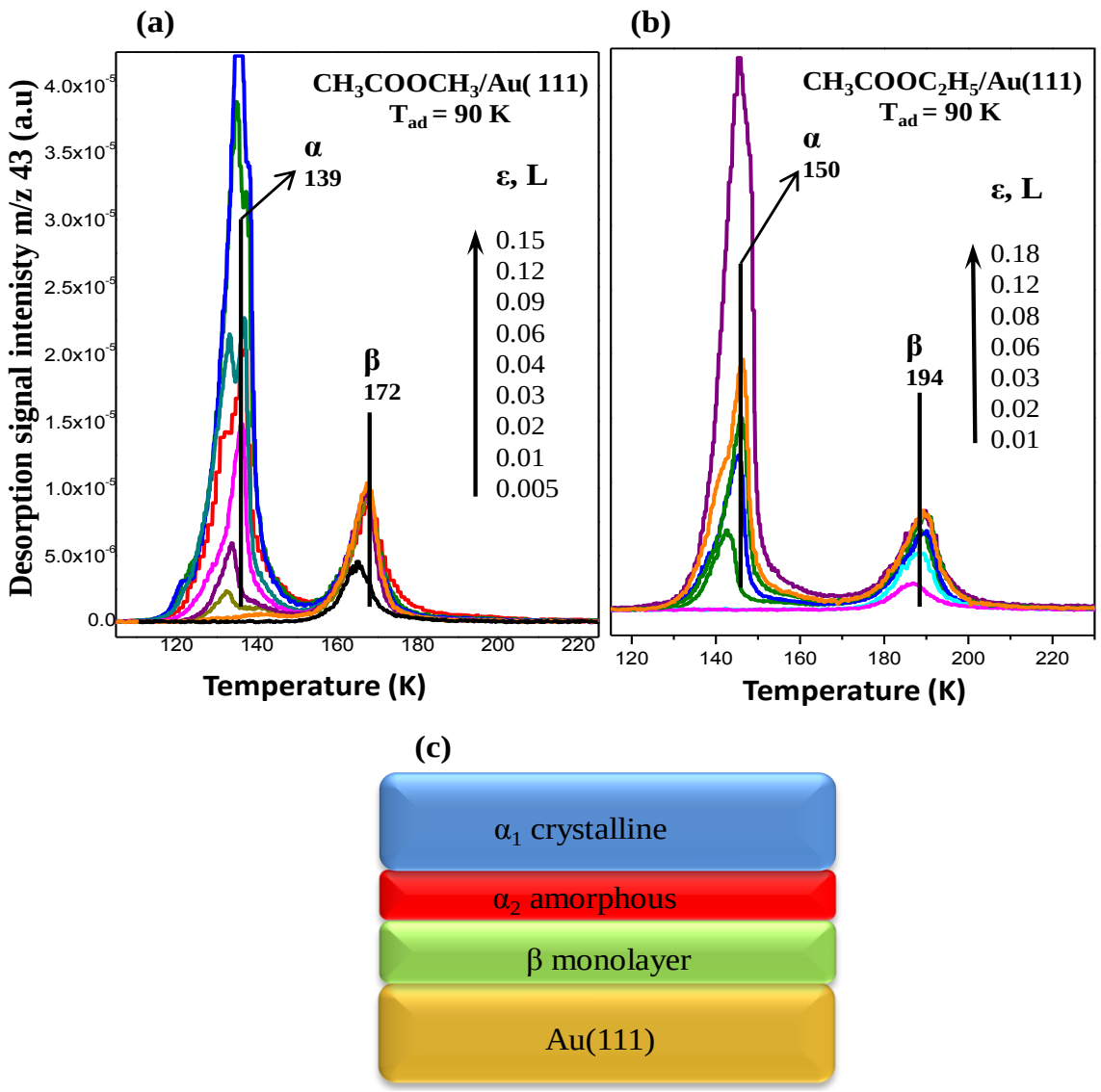

Figure 42. TPD spectra corresponding to various exposures of (a) methyl acetate and (b) ethyl acetate dosed onto clean Au(111) at 90 K. (c) schematic representation of desorption behavior.

3.2.6 Desorption Energy Trends of the Organic Adsorbates Studied in the Current Study

Redhead method has been used to calculate the desorption activation energies of the first monolayer of the various oxygenates on Au(111) that have been studied in the current work. *Figure 43* indicates that the desorption energy increases as we move towards left. A higher desorption energy means that the adsorbate will tend to stay on the Au(111) surface for a longer time. The longer the residence time, the higher will be the porbability of adsorbate towards total oxidation. As we can see, 1-propanol (n-propanol) has the highest desorption

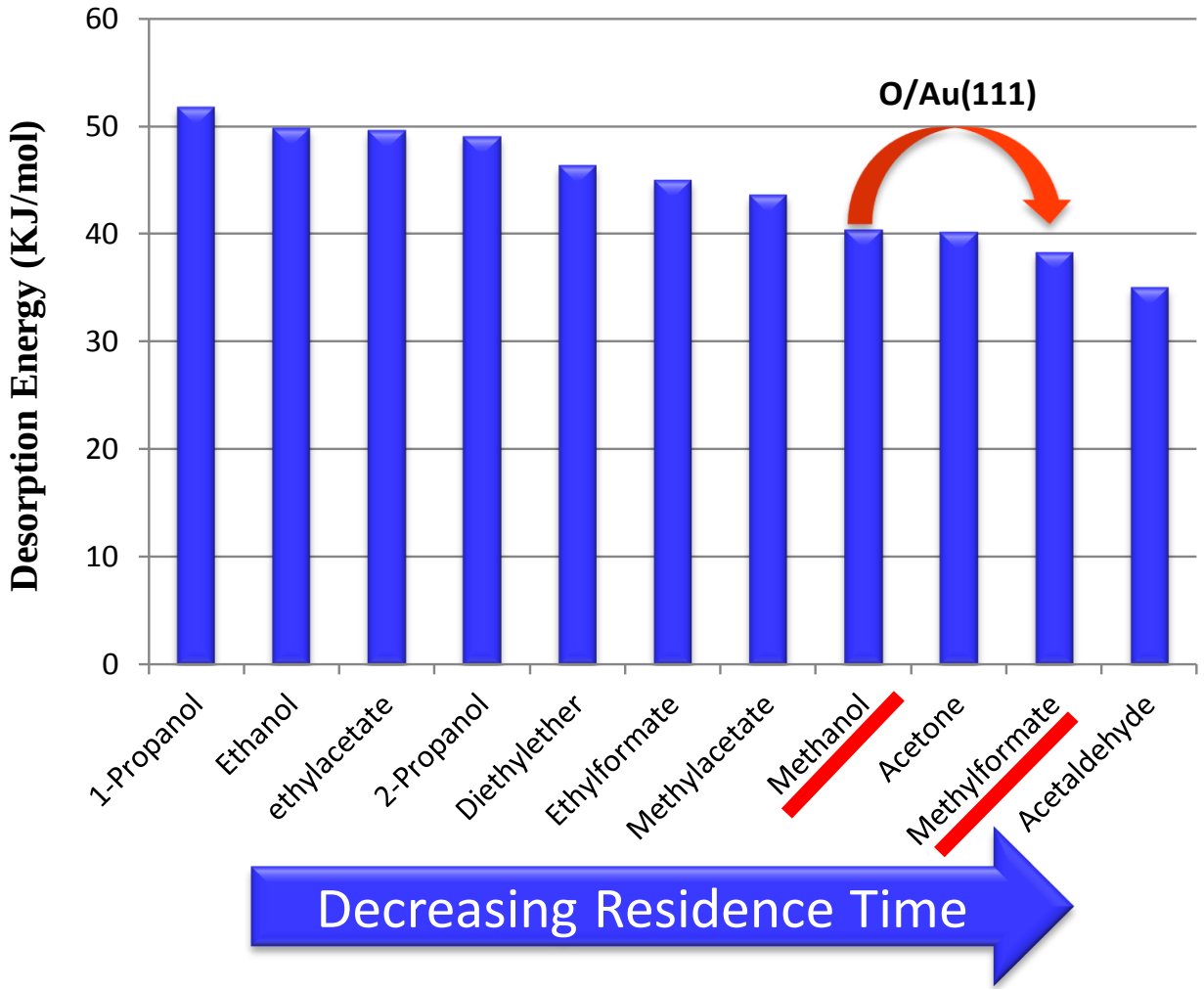

Figure 43. Desorption energies of the investigated organic molecules on the Au(111) single crystal surface

energy, which means that the 1-propanol has a strong interaction with the surface and will stay on the surface for a long time. If one of the oxidation products during a reaction has a lower residence time, it will leave the surface easily and a valuable partial oxidation product will be

obtained rather then the total combustion product (i.e. CO_2). Desorption energy trends from the *Figure 43* can help us in predicting the most probable partial oxidation products in an oxidative coupling or partial oxidation reaction.

Figure 44(a) and *(b)* reveal that each class of compound shows some trends related to the chain length. The desorption energy increases with the increase in chain length as shown in *Figure 44*. For example, in alcohols, methanol has a lower molecular mass than the 1-propanol so its desorption energy is less than 1-propanol. This indicates that alkyl group share its electrons through the inductive effect with oxygen atom bonded to the electrophilic gold atoms. The increase in the chain length increases this effect and makes the interaction much stronger. Furthermore, increasing chain length also increases Van der Waals interactions thereby increasing adsorption strength. Similarly, esters also show similar trends between desorption energy and chain length/molecular mass.

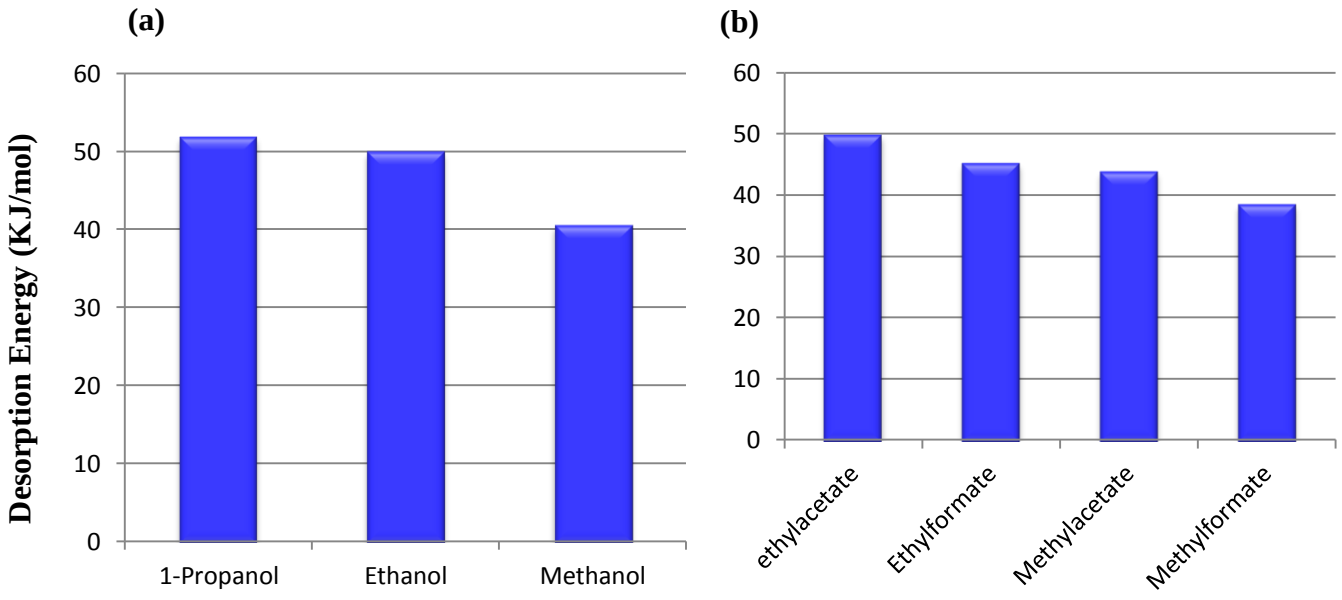

Figure 44. Desorption energy trends among (a) alcohols and (b) esters as a function of the chain length.

Partial oxidative coupling reaction of methanol on O(ad) covered Au(111) surface has been also carried out as a justification of the current hypothesis *(Figure 45)*. As predicted from *Figure 43*, the desorption energy for methanol is higher than its products, which are methyl formate and formaldehyde. The methyl formate will desorb immediately as it is formed because of its low desorption energy. Observation of methyl formate and formaldehyde as the major oxidation products of methanol on Au(111) justifies the selectivity forecasting approach discussed above. Thus, these results suggest that desorption energy trends of organic compounds may greatly assist us towards estimating the selectivity of model catalysts towards a particularly desired product.

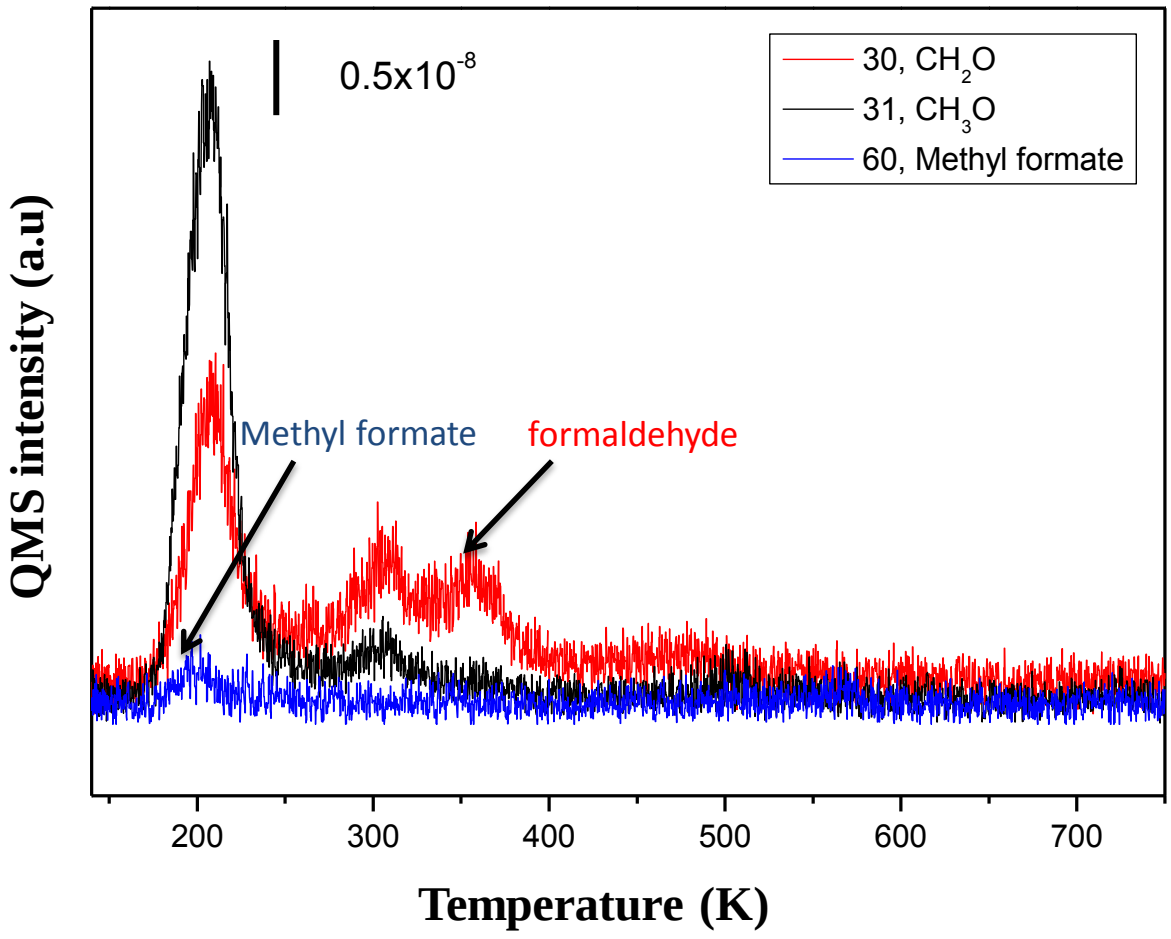

Figure 45 TPD data for the partial oxidative coupling reaction of Methanol/O/Au(111) at 140 K.

Hypothesis works

We have originally proposed a hypothesis that can be summarized as:

'Selectivity of Au(111) single crystal catalysts in a Partial Oxidation (PO) Reaction strongly depends on the adsorption energy of this particular molecule on the clean Au(111) surface"

Our current findings indicate that the proposed hypothesis is at least valid for the investigated reaction, where methanol partial oxidation with adsorbed atomic oxygen selectively yielded, methylformate, formaldehyde as partial oxidation products in addition to CO_2 as the total oxidation product. Calculated desorption energy trend reveals very good agreement with the selectivity of the partial oxidation reaction of methanol.

4. CONCLUSION

Adsorption and desorption behavior of various oxygenates i.e alcohols, aldehydes, ethers, ketones, and esters were systematically investigated over Au(111) single crystal model catalyst surface. Most of these organic chemicals do not typically show any decomposition on the Au(111) single crystal surface. This means that these compound have a very weak interaction with the Au(111) surface. In other words, adsorption/desorption is molecularly reversible. These compounds desorb typically in two states, i.e monolayer and multilayer (except for acetaldehyde) as a function of adsorbate coverage. Acetaldehyde polymerizes on the surface, revealing complex desorption signals at elevated temperatures.

The desorption energy values have been calculated through Redhead analysis of the TPD data. The desorption energy trends have been proposed to a be a useful descriptor for estimating the selectivity of the Au(111) model catalyst towards a particular partial oxidation product. Validity of this descriptor has been demonstrated in methanol partial oxidation on Au(111) where formaldehyde and methyl formate were experimentally observed to be the prominent oxidation products, in good agreement with the desorption energy trend analysis proposed in this study.

References

[1] X. H.; Xia, T.; Iwasita, F.; Ge, W.; Vielstich. *Electrochimica Acta*. **1996**, 41, 711-718.

[2] J.; Greeley, M.I.; Mavrikakis. *J.Am.Soc*, **2004**, 126, 3910-3919

[3] A.; Wittstock,V.; Zielasek,J.; Biener,C. M.; Friend,M.; Bäumer, *Science***.** , **2010**, 319, 327

[4] Principles and practice of heterogeneous catalysis, J.M.; Thomas, W.J.; Thomas. **1997**.

[5] P.L.J.; Gunter, J.W.; Niemantsverdriet, F.H.; Ribeiro, G.A.; Somorjai. *Catal. Rev.* **1997,** *39,* 77.

[6] J.; Libuda, H.J.; Freund, *Surf. Sci. Rep*. **2005**, *57*, 157.

[7] J.; Greeley, M.l.; Mavrikakis. *J.Am.Soc*, **2004**, 126, 3910-3919.

[8] H.J.; Freund, H.;Kuhlenbeck, J.; Libuda, G.; Rupprechter, M.; Baumer, H.; Hamann, *Top. Catal*. **2000**, *15*, 201.

[9] B.; Hammer, J. K.; Norskøv. *Nature*.**1995**, 376, 238–240.

[10] M.; Haruta, T.; Kobayashi, H.; Sano, N.; Yamada, *Chem. Lett*. **1987**, 405–408.

[11] M.; Haruta, N.; Yamada, T.; Kobayashi, S.; Iijima. *J.Catal*. **1989**, 115, 301

[12] T.; Hayashi, K.; Tanaka, M.; Haruta. *J.Catal*. **1998**, 178, 566.

[13] D.; Andreeva, V.; Idakiev, T.; Tabakova, A.; Andreev, R.; Giovanoli, *Appl.Catal. A*. **1996**, 134, 275.

[14] A.; Ueda, M. Haruta. *Gold Bull*. **1999**, 32, 3

[15] G.C.; Bond, P.A.; Sermon, G.; Webb, D. Buchanan, P.B.; Wells, *J. Chem. Commun*. **1973**, 444

[16] A. S. K.; Hashmi, G. J.; Hutchings. *Angew. Chem*. **2006**, 45, 7896–7936.

[17] B.K.; Minand, C.M.; Friend. *Chem. Rev.* **2007**, 107, 2709–2724.

[18] T.; Janssens, B.; Clausen, B.; Hvolbaek, H.; Falsig, C.; Christensen, T.; Bligaard, J.; Norskov, Top. Catal. **2007**, 44, 15-26.

[19] M.; Mihaylov, E.; Ivanova, Y.; Hao, K.; Hadjiivanov, H.; Knozinger, B.C.; Gates. *J. Phys. Chem* C. **2008,** 112, 18973.

[20] N.; Weiher, A.M.; Beesley, N.; Tsapatsaris, L.; Delannoy, C.; Louis, J.A.; van Bokhoven, S.L.M.; Schroeder. *J.Am.Chem. Soc.* **2007,** 129, 2240–2241.

[21] N.; Lopez, T.V.W.; Janssens, B.S.; Clausen, Y.; Xu, M.; Mavrikakis, T.; Bligaard, J.K.; Norskov. *J.Catal.* **2004**, 223-232

[22] B.; Hvolbaek, T.V.W.; Janssens, B.S.; Clausen, H.; Falsig, C.H.; Christensen, J.K.; Norskov. *Nano Today* **2007,** 2-14

[23] J.A.; van Bokhoven. *Chimia.* **2009,** 63-257

[24] A.P.; Alivisatos. Semiconductor Clusters, Nanocrystals, and Quantum Dots.Science. **1996**, 271, 933-937.

[25] M.; Brust, C. J.; Kiely. Colloids Surf. A: Physicochem. Eng. Asp. **2002**, 202, 175-186.

[26] R. P.; Andres, T.; Bein, M.; Dorogi, S.; Feng, J. I.;J enderson, C. P.; Kubiak, W.; Mahoney, R. G.; Osifchin, R.; Reifenverger, *Science*. **1996**, 272, 1323-1325.

[27] N.; Lopez, J.K.; Nørskov. *J. Am. Chem. Soc*. **2002**, 124, 11262–11263.

[28] M.; Mavrikakis, P.; Stoltze, J.K.;Nørskov. *Catal. Lett*. **2000**, 64, 101–106.

[29] C.; Lemire, Meyer, R.; Shaikhutdinov, Sh.K.; Freund, H.-J.Surf. Sci.2004,552, 27–34

[30] M.; Boronat, A. L.; Perez, A.; Corma. *Accounts of Chemical Research. **2014***, 47, 834-844.

[31] S.; Chretien, S. K.; Buratto, H.; Metiu. *Current Opinion in Solid State and Materials Science.* **2007**, 11, 62-75.

[32] M.; Valden, X.; Lai, D.W.; Goodman. *Science*. **1998**, 281,1647

[33] A. R.; Sandy, S. G. J.; Morchrie, D. M.; Zehner, K. G. Huang, D.; Gibbs. *Phys. Rev*. B. **1991**, 43, 4667.

[34] M.; Mavrikakis, P.; Stoltze, J. K.; Norskov. *Catal. Lett*. **2000**, 64, 101

[35] S.; Chretien, M.S.; Gordon, H.; Metiu. *J.Chem.Phys*. **2004**, 121, 3756-66.

[36] J.V.; Barth, H.; Brune, G.; Ertl, R.J.; Behm, *Phys. Rev. B*, **1990**, 42, 93.

[37] N.; Takeuchi, C.T.; Chan, K.M.; Ho. *Phys. Rev. B* **1991**,43, 13899.

[38] A.Y.; Lozovoi, A.; Alavi. *Phys. Rev. B*, **2003**, 68, 18.

[39] Z.; Crljen, P.; Lazic, D.; Sokcevic, R. Brako. *Phys. Rev. B*. **2003**, 68, 8.

[40] S. R.; Bare, G. A.; Somorjai. Surface chemistry.

[41] http://www.fhi-berlin.mpg.de/∼hermann/Balsac/SSDpictures.html#A

[42] R. Masel, Principles of Adsorption and Reaction on Solid Surfaces, JohnWiley & Sons, **1996**, 38

[43] V.; Heine, L.D.; Marks, *Surf. Sci*, **1986**, 165, 65.

[44] M.M.; Dovek, C.A.; Lang, J.; Nogami, C.F.; Quate, *Phys. Rev. B.***1989**, 11, 973

[45] M.A.; van Hove, R.J.; Koestner, P. C.; Stair, J. P.; Biberian, L. L.; Kesmodel, I.; Bartos, G.A.; Somorjai, *Surf. Sci*. **1981**, 103, 189.

[46] E. I.; Batanouny, M.; Burdick, S.; Martini, K. M.; Stancioff. *Phys. Rev. Lett*. **1987**, 58, 2762

[47] C.P.; Vinod, J.W.N.; Hans, B.E.; Nieuwenhuys. *Appl.Catal. A*, **2005**, 291, 93.

[48] Y.; Okamoto, Chem.Phys.Lett. **2005**, 405, 79

[49] M.E.; Bartram, B.E. Koel, Surf.Sci. **1989**, 213, 137

[50] W.H.; Zhang, Z.Y.; Li, Y.; Luo, J.L.; Yan,J. Chem. Phys. **2008**, 129, 134708

[51] G.N.; Kastanas, B. E.; Koel, Appl. Surf. Sci.**1993**, 64, 235.

[52] Liu, G.; Rodriguez, J. A.; Dvorak, J.; Hrbek, J.; Jirsak, T.Surf. Sci.**2002**, 505, 295.

[53] Z. J.; Sun, S.; Gravelle, R. S.; Mackay, X. Y.; Zhu, J. M.;White. *J. Chem. Phys*. **1993**, 99, 10021.

[54] M.; Polcik, L.; Wilde, J.; Haase, B.; Brena, D.; Cocco, G.; Comelli, G.; Paolucci. *Phys. Rev*. *B.* **1996**, 53, 13720.

[55] G. J.; Jackson, S. M.; Driver, D. P.; Woodruff, N.; Abrams, R. G.; Jones, M. T.; Butterfield, M. D.; Crapper, B. C. C.; Cowie, V.; Formoso. *Surf. Sci*. **2000**, 459, 231.

[56] R.; Meyer, C.; Lemire, S. K.; Shaikhutdinov, H.; Freund, *Gold Bull*. **2004**, 37, 72.

[57] K. F.; Peters, P.; Steadman, H.; Isern, J.; Alvarez, S.; Ferrer, *Surf. Sci*. **2000**, 467, 10.

[58] L.; Piccolo, D.; Loffreda, F. J.; Cadete Santos Aires, C.; Deranlot, Y.; Jugnet, P.; Sautet, J. C.; Bertolini. *Surf. Sci*. **2004**, 566,568-995.

[59] D. A.; Outka, R. J.; Madix. *Surf. Sci*. **1987**, 179, 351.

[60] J. M.; Gottfried, K. J.; Schmidt, S. L. M.; Schroeder, K.; Christmann. *Surf. Sci.* **2003**, 536, 206.

[61] A.; Sandell, P.; Bennich, A.; Nilsson, B.; Hernnas, O.; Bjorneholm, N.;Martensson, *Surf. Sci*. **1994**, 310, 16.

[62] J.H.; Kim, E.; Samano, B. E.; Koel, *J. Phys. Chem. B.* **2006**, 110, 17512.

[63] D. A.; Outka, R. J.; Madix,. *J. Am. Chem. Soc*.**1987**, 109, 1708.

[64] M. A.; Chesters, G. A.; Somorjai, *Surf. Sci*.**1975**, 52, 21.

[65] K. A.; Davis, D. W.; Goodman, *J. Phys. Chem. B*. **2000**,104, 8557.

[66] S.; Chretien, M. S.; Gordon, H.; Metiu, *J. Chem. Phys*. **2004**, 121, 3756.

[67] S. M.; Wetterer, D. J.; Lavrich, T.; Cummings, S. L.; Bernasek, G.; Scoles, *J. Phys. Chem. B*. **1998**, 102, 9266.

[68] R. J.; Baxter, G.; Teobaldi, F.; Zerbetto, *Langmuir.* **2003**, 19, 7335.

[69] M. A.; Lazaga, D. T.; Wickham, D. H.; Parker, G. N.;Kastanas, B. E.; Koel, *ACS Symp. Ser*.**1993**, 523, 90.

[70] D. A.; Outka, R. J.; Madix, *Surf. Sci*.**1987**, 179, 361.

[71] J. L.; Gong, C. B.; Mullins*, J. Am. Chem. Soc*.**2008**, 130, 16458.

[72] J.L.; Gong, D. W.; Flaherty, R. A.; Ojifinni, J. M.; White, C. B.; Mullins.*J. Phys. Chem. C*. **2008**, 112, 5501.

[73] R. J.; Madix, C. M.; Friend, X. Y.; Liu. *J. Catal*. **2008**, 258, 410.

[74] C. P.; Vinod, J. W.; Niemantsverdriet, B. E.;Nieuwenhuys. *Phys. Chem. Chem. Phys*. **2005**, 7, 1824.

[75] D.; Syomin, B. E.; Koel, *Surf. Sci*. **2002**, 498, 53.

[76] M.; Chtaib, P. A.; Thiry, J. P.; Delrue, J. J.; Pireaux, R.J. Caudano. *Electron Spectrosc. Relat. Phenom*. **1983**, 29, 293.

[77] M.; Chtaib, P. A.; Thiry, J. J.; Pireaux, J. P.; Delrue, R.; Caudano, *Surf. Sci*. **1985**, 162, 245.

[78] J. H.; Kim, B. E.; Koel. *Langmuir*. **2005**, 21, 3886.

[79] A.G.; Sault, R.J.; Madix, C.T.; Campbell. Surf. Sci.**1986**, 169, 347.

[80] Shishakov, N. A.J. Phys. Chem.**1960**, 64, 1580.

[81] Legare, P.; Hilaire, L.; Sotto, M.; Maire, G. Surf. Sci.**1980**, 91, 175.

[82] Pireaux, J.J.; Chtaib, M.; Delrue, J.P.; Thiry, P.A.; Liehr, M.; Caudano, R.Surf. Sci.**1984**, 141, 211.

[83] J. J.; Pireaux, M.; Liehr, P. A.; Thiry, J. P.; Delrue, R.;Caudano, *Surf. Sci*, **1984**, 141, 221.

[84] D. H.; Parker, B. E.; Koel, *J. Vac. Sci. Technol. A*. **1990**, 8, 2585.

[85] T. A.; Baker, C. M.; Friend, E.; Kaxiras. *J. Phys. Chem. C*, **2009**, 8, 113.

[86] J.; Gong, chem. review JACS. **2012**, 112. 2987.

[87] Xu, B.; Liu, X.; Haubrich, J.; Friend, C. M. Nat. Chem. **2009**, 2, 61.

[88] B.; Xu,R. J.; Madix, C. M.; Friend. *Accounts of Chemical Research.* **2014**, 47, 761–772.

[89] B.; Xu,R. J.; Madix, C. M.; Friend. *J. Am. Chem. Soc.* **2011**, 133, 20378–20383

[90] Gong, J. L.; Mullins, C. B.J. Am.Chem. Soc. **2008**, 130, 16458.

[91] Xu, B.; Zhou, L.; Madix, R. J.; Friend, C. M.Angew. Chem. **2010**, 49, 394.

[92] J.T.; Roberts, R.J.; Madix, W.W.; Crew. J. Cat al. **1993**,141, 300.

[93] W. X.; Huang, J. M.; White, Catal. Lett. **2002**, 84, 143.

[94] X. Y. Deng, B. K. Min, X. Y. Liu and C. M. Friend,J. Phys. Chem. B. **2006**, 110, 15982

[95] Hakkinen, H.; Landman, U.J.; Am. Chem. Soc. **2001**, 123, 9704.

[96] Outka, D. A.; Madix, R. J.Surf. Sci.**1987**, 179, 351.

[97] A.; Wittstock, V.; Zielasek, J.; Biener, C.M.; Friend, M.; Baumer. Science **2010**, 327, 319

[98] A.; Wittstock, V.; Zielasek, J.; Biener, C.M.; Friend, M.; Baumer. Science **2010**, 327, 319.

[99] Woodruff, D.P.; Delchar, T.A. *Modern Techniques of Surface Science*, 2nd Edition, Cambridge University Press, Cambridge, **1994**.

[100] O'Hanlon, J.F. *A User's Guide to Vacuum Technology*, 3rd Edition, Wiley, New Jersey, **2003**.

[101] Behrisch, R.; Eckstein, W. *Top. Appl. Phys.* **2007**, *110*, 1.

[102] Jona, F.; Strozier, J.A.; Yang, W.S. *Rep. Prog. Phys*. **1982**, *45*, 527.

[103] Atkins, P; de Paula, J. *Physical Chemistry*, 8th Edition, Oxford University Press, Oxford, **2006**.

[104] Van Hove, M.A.; Weinberg, W.H.; Chan, C.M. *Low Energy Electron Diffraction*, Springer Verlag, Berlin, **1986**

[105] Niemantsverdriet, J.W. *Spectroscopy in Catalysis*, 3rd Edition, Wiley, Mörlenbach, **2007**.

[106] Clarke, L.J. *Surface Crystallography*, Wiley, New York, **1985**

[107] Rodriguez, J.A.; Jirsak, T.; Liu, G.; Hrbek, J.; Dvorak, J.; Maiti, A. *J. Amer. Chem. Soc*. **2001**, *123*, 9597.

[108] Riviere, J.C. *Surface Analytical Techniques*, Oxford Science Publications, Oxfordshire, **1990.**

[109] Simon J. Garrett. *Special Topics in Analytical Chemistry*. 2001.

[110] P.A Redhead vacuum **1962,** 12, 203-2011.

[111] B. Xu, X. Liu, J. Haubrich, R.J. Madix, C.M. Friend, *Angew. Chem. Int. Ed.* **2009**. 48, 4206.

[112] B. Xu, R.J. Madix, C.M. Friend, *J. Am. Chem. Soc*. **2010**. 132 16571

[113] B. Xu, J. Haubrich, T.A. Baker, E. Kaxiras, C.M. Friend, *J. Phys. Chem. C.* **2011**. 115, 3703

[114] H.; Nakamura, T.; Mantoku, T.; Furukawa, Fujitani. *J. Phys. Chem. C* **2011**, 115, 16074–16080.

[115] I.; Horcas, R. Fernández, J. M. G. R.; Colchero, J. G. J.; Herrero, A. M.; Baro. *Rev. Sci. Instrum.* **2007**, 78, 013705

[116] J.; Gong, D. W.; Flaherty, R. A.; Ojifinni, J. M.; White,C. B.; Mullins. J. *Phys. Chem. C.* **2008**,112,5501-5509.

[117] J.; Gong, C. B.; Mullins. *J. Am. Chem. Soc.* **2008**, 130, 16458–16459.

[118] J.; Gong, D. W.; Flaherty, T.; Yan C. B.; Mullins. *Chem.Phys.Chem* **2008**, 9, 2461 – 2466.

[119] W. S.; Sim, P.; Gardner, D. A.; King. *J. Am. Chem. Soc.* **1996**, 118, 9953.

[120] Y. Bu, J. Breslin, and M. C. Lin J. Phys. Chem. B1997,101,1872-1877

[121] O. A.; Belyakova, Yu. L.; Slovokhotov. *Russ. Chem. Bull*. **2003**, 52, 11.

[122] http://webbook.nist.gov/chemistry/